Development of a test station for the characterization of Silicon Photo-Multipliers in liquid xenon environment

von

Daniel Wenz

Bachelorarbeit in Physik
vorgelegt dem Fachbereich Physik, Mathematik und Informatik (FB 08)
der Johannes Gutenberg-Universität Mainz
am 16. Juni 2015

1. Gutachter: Prof. Dr. Uwe Gerd Oberlack
2. Gutachter: Prof. Dr. Michael Wurm

Ich versichere, dass ich die Arbeit selbstständig verfasst und keine anderen als die angegebenen Quellen und Hilfsmittel benutzt sowie Zitate kenntlich gemacht habe.

Mainz, den

Daniel Wenz
ETAP/XENON
Institut für Physik
Staudingerweg 7
Johannes Gutenberg-Universität D-55099 Mainz
dwenz@students.uni-mainz.de

Entwicklung eines Teststands zur Charakterisierung von Silizium Photomultiplier in flüssig Xenon

Seit nun rund 50 Jahren werden flüssig Xenon Detektoren erfolgreich eingesetzt. Bisher verwendet man zum detektieren des tief ultraviolettem Lichts ($\sim$175 nm) sogenannte Photomultiplier.

Jedoch wurde in den letzten Jahren eine neue vielversprechende Art von Halbleiterphotosensoren entwickelt. Diese basieren auf dem physikalischen Konzept von Avalanche Photodioden und heißen Silizium Photomultiplier (SiPMs). Wegen ihrer hohen Quanteneffizienz, hohen Verstärkungsfaktor bei geringer Versorgungsspannung und gute Zeitauflösung, um nur ein paar Eigenschaften hier zu nennen, lösen sie in immer mehr Experimenten die herkömmlichen Photomultiplier ab. Als erste Firma hat sich Hamamatsu Photonics in Kollaboration mit dem MEG Experiment der Herausforderung gestellt Silizium Photomultiplier auch für tief ultraviolettes Licht zu entwickeln. Auch andere Hersteller, wie das deutsche Unternehmen Ketek, haben ihr Interesse an solch einer Entwicklung bekundet und sind mit uns eine Kollaboration eingegangen.

Im diesem Zuge behandelt meine Bachelorarbeit die Entwicklung, den Aufbau und die Erstmessung eines Teststandes zur Charakterisierung von Silizium Photomultiplier in flüssig Xenon.

Hierzu wurde ein bereits existierendes System, welches zur Charakterisierung von sogenannten Large Area Avalanche Photodioden benutzt wurde, wieder verwendet. Jedoch musste dies für die Benutzung der Silizium Photomultiplier leicht verändert werden. Darüber hinaus wurde während dieser Bachelorarbeit eine neue Messeinheit entwickelt welches speziell auf die Charakterisierung von mehreren SiPMs gleichzeitig zugeschnitten wurde. Für unseren ersten Testdurchlauf wurde uns ein ausgemustertes Exemplar der MEG SiPMs von Hamamatsu gratis zur Verfügung gestellt.

Die Entwicklung wurde durch eine Simulation, welche von der Arbeitsgruppe bereit gestellt wurde unterstützt. Ferner wurde sie mit einem analytischen Ansatz zur Bestimmung der Beleuchtungsstärke verglichen. Des Weiteren wird zur Bestimmung der "Photon Detection Efficiency" im Rahmen dieser Arbeit eine kurze Analysemethode vorgestellt. Das Ziel war es diesen Ansatz auf die Erstdaten des Testdurchlaufs anzuwenden und dadurch die gemessenen Beleuchtungsstärke mit der Simulation zu vergleichen. Eine kurze Präsentation der Daten und der Resultate befinden sich ebenfalls gegen ende dieser Arbeit.

Contents

1 Introduction

During the last 50 years liquid xenon detectors has assumed an important role in science. They are used in particle physics and astrophysics but also they are starting to be employed in medical diagnostics. Due to its excellent behavior as scintillation medium and a good absorption power in addition with the possibility to scale them to a large sensitive volumes, liquid xenon is largely used in rare event detection. Like dark matter search and neutrino-less double-beta decays, just to mention some. Furthermore liquid noble scintillators provide, compared to other liquid scintillators, the unique feature to produce charge carriers in addition to scintillation photons. This can be exploit by specific detectors to acquire an additional signal simultaneous to the scintillation light.

In the last few years many modern scintillation detectors took the advantage of a new type of solid state sensors. Those so-called Silicon Photo-Multipliers (SiPM) exhibit an high quantum efficiency, high gain at low operating voltages, a good time resolution and insensitivity to high magnetic fields. Furthermore do they have a comparable small size in respect to other photon counting devices, like vacuum photo-multiplier tubes which means a higher granularity. The use of SiPMs in liquid xenon applications is still challenging due to the fact that the Vacuum Ultra Violet (VUV) light ($\sim$175 nm) that is produced is absorbed within the first few insensitive nm of the device. The first device which is operating in this spectral range was developed by the MEG experiment [8] in collaboration with Hamamatsu Photonics. Also other companies like Ketek in Germany accept the challenge and trying to develop there own devices.

This thesis tries to join the effort and deals with the development of a test system for the characterization of new VUV sensitive SiPM prototypes in a liquid xenon environment.

Chapter 2 deals with the theoretical foundations to understand the operating principle of a SiPM and the scintillation process in liquid xenon. We had the advantage to reuse an already existing test system which was used for the characterization of Large-Area Avalanche Photo-Diodes (LAAPD) in liquid xenon. The experimental system and the applied minor modifications are described in chapter 3, while the analysis approach, such as determining the detection efficiency and the illumination yield, are described in chapter 4. Furthermore this chapter includes a brief presentation and discussion of the first results from the initial test-run. At the same time we design also a new measurement set-up specialized for the characterization of SiPMs in liquid xenon. In addition to Hamamatsu SiPMs, it provides the possibility to test SiPMs from another supplier, Ketek GmbH, who started a collaboration with us. This is introduced in chapter 5.

2 Theoretical foundations

2.1 Semiconductors

Semiconductors are materials that behave like an electrical insulator for low and as a weak conductor for high temperatures (fig. 2.1). Most of the elements within the fourth to the sixth column of the periodic table are pure semiconductors. They all have in common a fully occupied valence band and an unoccupied conduction band (at a temperature of 0 K). The band gap between valence and conducting band is typically in the magnitude of some eV (1, 11 eV at 300 K for Si [1]). Hence it is easy to lift an electron from the valence to the conducting band, either by thermal excitation (e.g. phonons) or the photoelectric effect. Whenever such an excitation happens, each excited electron also leaves a so-called "hole" in the valence band, which can be effectively interpreted as a positive charge (shown in fig. 2.2). The electron and hole have equal densities and they are called intrinsic charge carriers. The density n_i caused by thermal excitation can be derived from the Fermi function and is given by [1]

$$\begin{aligned} n_\mathrm{i} &= n = p \qquad\qquad \text{with } n \text{ electron \& } p \text{ hole density} \\ \Leftrightarrow n_\mathrm{i} &= \sqrt{n \cdot p} \\ &= c(m_\mathrm{e}^*, m_\mathrm{p}^*) \cdot T^{\frac{3}{2}} \cdot e^{-\frac{E_\mathrm{g}}{2k_\mathrm{B}T}} \end{aligned} \tag{2.1}$$

with a constant $c(m_\mathrm{e}^*, m_\mathrm{p}^*)$, that basically depends on the effective mass for electrons and holes, the energy gap E_g, the Boltzmann constant k_B and the temperature T. Whereby the effective mass is the mass a particle seems to have during its trajectory trough a solid. It is defined like normal mass in Newton's second law.
Without an electrical field applied to the semiconductor, the holes and electrons recombine after a while, but if an electric field is applied, the electrons and holes drift to the electrodes. The resulting current is then given by the so-called intrinsic conduction.

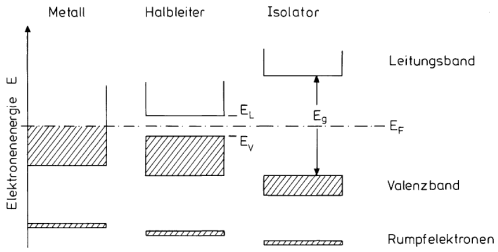

Fig. 2.1: Sketch for different material. From the left to the right the band structures of conductors (Metall), semiconductors (Halbleiter) and insulators (Isolator) at 0 K are sketched. The white areas are the conducting bands (Leitungsband) and the shaded areas the valence bands (Valenzband). ([3] page 403, fig.12.1.)

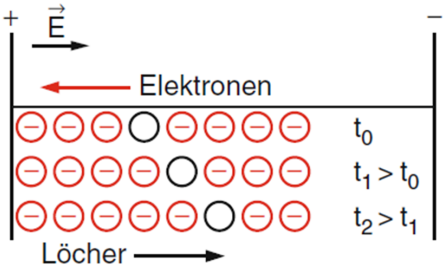

Fig. 2.2: Illustration of electron-hole (Elektron-Löcher) conduction caused by an applied voltage. While the electrons drift to the anode, the respective holes seems to "drift" to the cathode. ([1] page 487 , fig. 14.6.)

More interesting for electrical devices are the so called doped semiconductors. Doped means that some of the pure semiconductor atoms, for example Si atoms, are replaced by atoms of the third or fifth column of the periodic table. A usual magnitude of this impurity concentration is 10^{-8} to 10^{-4} [1]. Because of the tetravalent covalently joined binding structure of pure silicon, impurities of the third and fifth column change the characteristics differently. A doping with pentavalent atoms produces a weakly bounded electron, thus the atom becomes a electron donor (n-type). On the other hand if the the pure silicon is doped with trivalent atoms it lose one binding electron, hence it causes a positive electron "trap" and becomes a electron acceptor (p-type). The binding energy of those acceptors and donors are slightly different to the energy of the valence and conducting band, so there are additional energy levels within the band structure compared to pure semiconductors. (fig. 2.3 and 2.4).

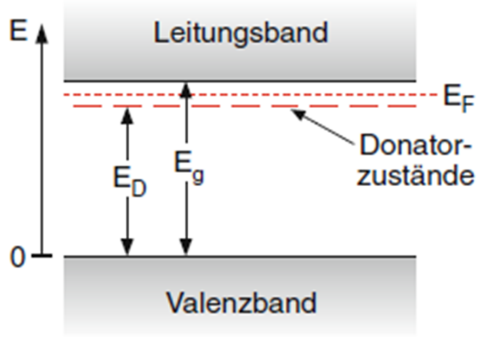

Fig. 2.3: Band structure of an n-type semiconductor at 0 K. The donor electrons can be easily excited from the donor level (Donatorzustände) to the conducting band (Leistungsband) by an energy of $\Delta E = E_g - E_D$. ([1] page 491, fig. 14.13.)

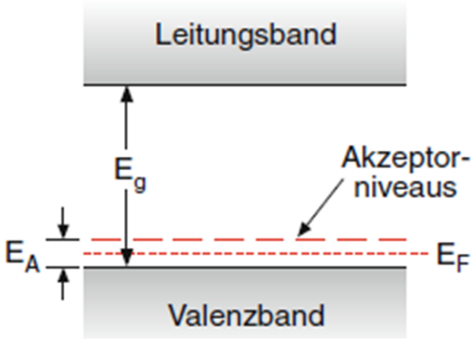

Fig. 2.4: Band structure of a p-type semiconductor at 0 K. The energy difference between the acceptor level E_A (Akzeptorniveaus) and valence band (Valenzband) is much smaller, than the energy gap E_g of the semiconductor. So an electron from the valence band can be caught easily. ([1] page 491, fig. 14.14.)

Because of those additional energy levels the behavior and the conductivity of the semiconductors change. In the case of an n-type semiconductor the electrons of the donor level are additionally excited, thus there are more electrons which contribute to the current than holes. So the electrons become the majority charge carriers and the holes the minority charge carriers.
In the case of the p-type semiconductor it is reversed. Because of the small energy difference E_A some electrons are caught in the acceptor level. Hence there is a surplus of holes in the semiconductor. Now the electrons become the minority charge carriers and the holes are the majority charge carriers.
Because of those additional holes or electrons the conductivity of doped semiconductors is already given by small temperatures like room temperature and is much higher than for intrinsic conductors. It can be divided into 3 regions like in figure 2.5 show.

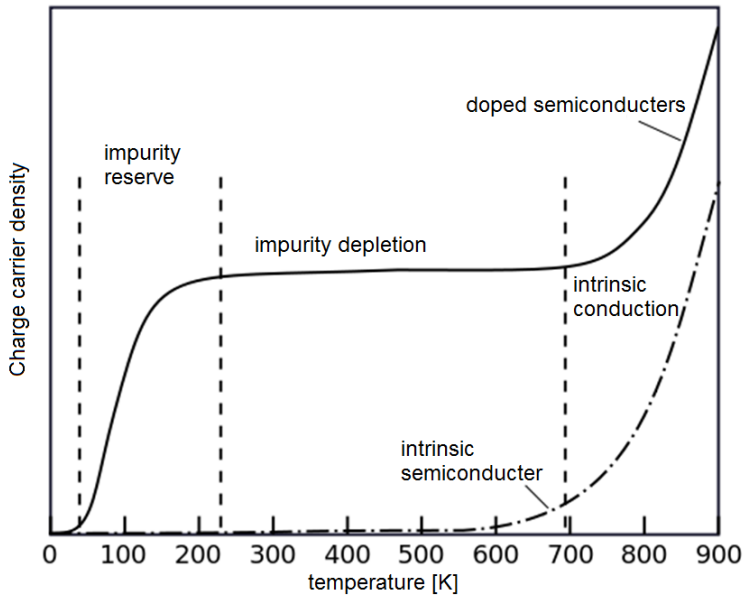

Fig. 2.5: Comparison of the conductivity between a doped and an intrinsic semiconductor. The dashed lines separate the different regions. [17]

The first region (impurity reserve) shows the rising of charge carry density of a doped semiconductor. This is caused by the excitation of the donor electrons into the conducting band (or by the generation of a hole by lifting valence electrons into the acceptor levels) of n-doped (or p-doped) semiconductors. If the impurity levels are depleted the charge density stays the same (second region) until the thermal energy is high enough to lift valance electrons into the conducting band and the density starts rising further (third region). Hence the conductivity of doped semiconductors is much higher.

Most modern electronic devices are based on a combination of p- and n-doped semiconductors. The easiest device of this kind is a diode. It is a single crystal which is p-doped on the one side and n-doped on the other. The junction between these both doped parts is called p-n junction. Within this p-n junction a gradient between the majority charge carrier concentrations gives rise to a diffusion current, which applies a so called space charge region or depletion zone. Inside this space charge region the donor electrons and acceptor holes recombine with each other and leave their donors and acceptors. Thus an electrical field is established within the space charge region, that produces a reversed operating current (drift current) and a potential energy shift of the band structure (fig. 2.6 and 2.7). After a while an equilibrium is reached.

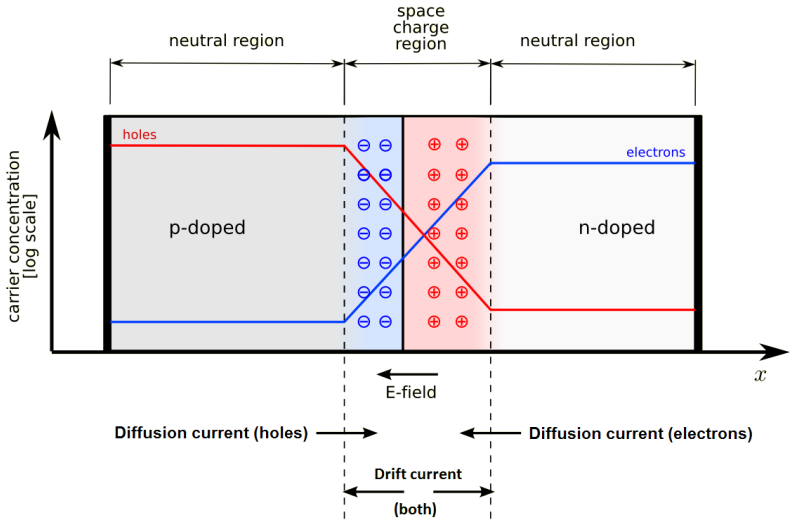

Fig. 2.6: Sketch of a p-n junction in equilibrium. Plotted is the carrier concentration for holes (red line) and electrons (blue line), over the position inside the p-n junction. The red and blue areas indicate the donors and acceptors left within the space charged region. The greater donor area (red) indicates a higher p doping. [18]

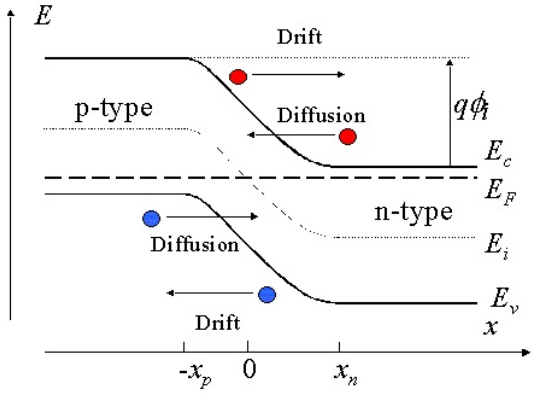

Fig. 2.7: Shown is the band structure of a p-n junction. The dots indicate the trajectory of the electrons (blue) and the holes (red). E_c indicates the energy of the conducting band, E_v the valence band energy. Φ_i shows the potential shift between the band structure caused by the electrical field. [21]

There are two possible ways to apply DC voltage to the p-n junction (fig. 2.8). The first is to connect the n-doped side to the cathode and the p-doped side to the anode ($U_a > 0$) . So the potential difference drops and more carriers are able to contribute

to the current. The Diode or p-n junction is operating in forward bias.
The second option is to plug in the p-n junction reversed ($U_a < 0$). This causes a rise of the potential difference, which introduces a small cutoff current in the beginning. If the voltage is increased beyond the so-called "breakdown voltage", the current starts rising exponentially. The reason for this is shown in figure 2.9. The potential difference decreases the n-doped conducting band energy below the valence band energy of the p-doped region. So it is possible to have a so-called "tunnel current" between those two energy bands.

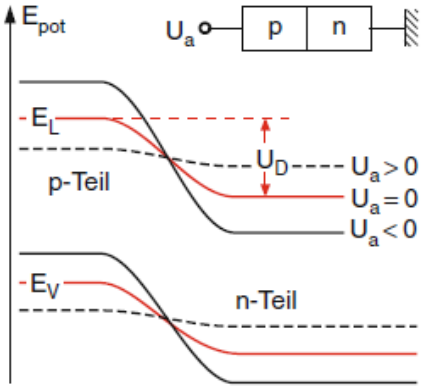

Fig. 2.8: The potential energy of a diode is shown with (black lines) and without (red line) any applied voltage U_a. The dashed black line shows the forward bias, meanwhile the straight line depicts the reverse bias. E_L is the conducting band energy and E_V is the energy of the valence band. ([1] page 495, fig. 14.17.)

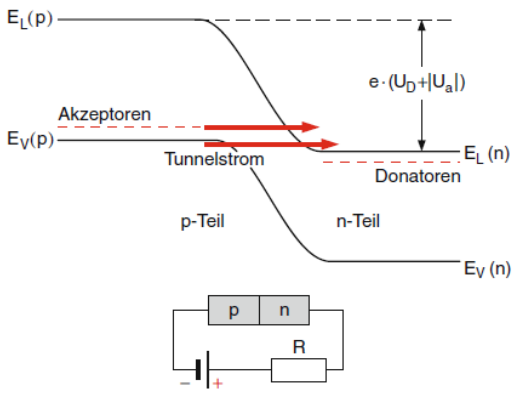

Fig. 2.9: The figure shows the tunnel current (Tunnelstrom) of a diode in reversed bias mode, which is supplied by a voltage that is in exceeding the break down voltage. ([1] page 495, fig. 14.19.)

2.2 Solid state photon sensors and avalanche photodiode

In order to detect photons the discussed properties of semiconductors can be used. If a photon impinging a semiconductor device, it transfers its energy to the bounded electrons exciting them into the conducting band, thus the increased charge carry density resulting in a measurable current signal. Hence a photon detection device based on this properties becomes possible.

An avalanche photodiode belongs to this type of devices. Its special layout has the additional feature to amplify the so-called avalanche, the current signal which is

produced by the absorbed photon. Hence even the detection of single photons becomes possible.

The most important characteristic of each photon counting device is the photon detection efficiency (PDE). It depends on the wavelength of the photons and is defined as

$$\mathrm{PDE}(\lambda) = \frac{\#\text{generated current pulses}}{\#\text{impinging photons}(\lambda)} \tag{2.2}$$

or rewritten with the so-called quantum efficiency (QE)

$$\mathrm{PDE}(\lambda) = \mathrm{QE}(\lambda) \cdot F \cdot \epsilon \tag{2.3}$$

whereby F is the ratio between the active device area compared to the total device area (the so-called fill factor) and ϵ the probability for an electron-hole pair to trigger an avalanche. The quantum efficiency is the probability that a photon generates an electron-hole pair within the intrinsic layer. It is determined by the reflection on the first layers and the protective coating and the absorption probability within the intrinsic layer.

A common layout for an APDs is the reach-through configuration [4]. It is basically structured as shown in figure 2.11. Photons enter the APD through a small layer of anti-reflective coating, followed by a tiny and highly p-doped layer. To achieve a high photon detection efficiency those layers should be as small as possible.
Subsequently the photon will be absorbed within the intrinsic layer, which is the thickest one to maximize the QE. For the charge carrier multiplication and the avalanche process high electrical field strengths are needed, hence the intrinsic layer is followed by a p- and a highly n-doped layer (fig. 2.10). Because of this high electrical fields the charge carriers acquire enough kinetic energy to excite additional bounded electrons to the conduction band. Hence a higher supplied voltage increases the amplification factor the so-called gain M which is explained subsequently.

To operate a APD as a photon sensor it must be reversed biased, so that the measured current is produced only by the absorbed photons. Two possible modes can be distinguished by the operating voltage V_{Bias}. If the voltage is below the breakdown voltage V_{Br} ($|V_{\mathrm{Bias}}| < |V_{\mathrm{Br}}|$), the APD is working as a proportional counter. That means, that each impact generates a number of charge carriers which is proportional, by a factor M which is called the "gain", to the number of incoming photons. This is a big advantage and allows an APD is able to measure even single photons.

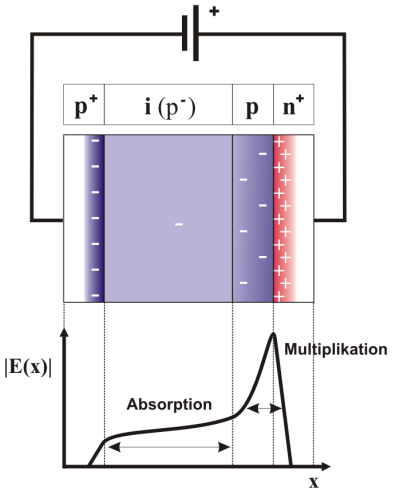

Fig. 2.10: Slices sketch of a reach-through configured APD. The different colors indicate the space charge density by the applied reverse voltage. Below the corresponding electrical field is plotted. [19]

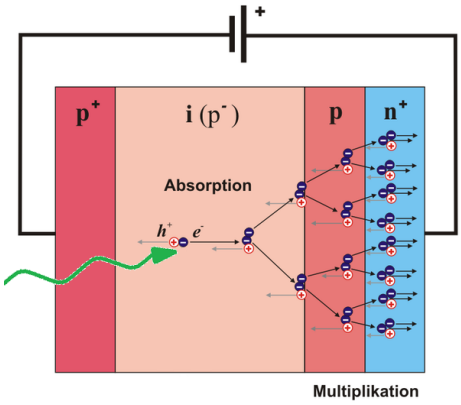

Fig. 2.11: Schematic of the multiplication process in an APD. The entering photon creates an electron hole-pair by the photoelectric effect, which is multiplied by collisions in the higher doped slices. [20]

If the operating voltage is increased beyond the breakdown voltage ($|V_{\mathrm{Bias}}| > |V_{\mathrm{Br}}|$) the APD is operating in the so-called Geiger mode (GM) and according to this the APD is called a GM-APD. In this mode each detected photon triggers an avalanche which results in a complete discharge of the APD. However, this is not very efficient for a normal APD, because of the complete discharge the signal is always the same independent if one, two or even more photons hit the APD.

2.3 Structure and operating principle of a SiPM

Hence the normal structure and size of a GM-APD is not efficient enough to count photons, it needs to be "dissected" in little pixels. Thus each pixel becomes an independent GM-APD with a size of the order of 50 μm. Since GM-APDs are blind for multiple photon hits, it is advisable to decrease the size of the pixels as far as possible.

To obtain a signal which is proportional to the number of absorbed photons they all have to be connected in parallel. Therefore the connection is done by a small substrate on the light sensitive side and a metal layer on the other side. To isolate the pixels a little gap in the order of 1 μm is between them. This device is now a silicon

photomultiplier.

The operating principle of such a SiPM can be sketched according to [6]. Each pixel of the SiPm can be described as a diode and a resistor connected in series. The resistor is called a quenching resistor R_{Q} and has the task to stop the avalanche and restore the pixel to the starting conditions. The diode can also be represented as a circuit shown in figure 2.12. Before the GM-APD is hit by a photon it can be described by a capacitance C_{D} which is charged at $V_{\mathrm{Bias}} > V_{\mathrm{Br}}$ and the quenching resistor R_{Q} (the switch is turned OFF).

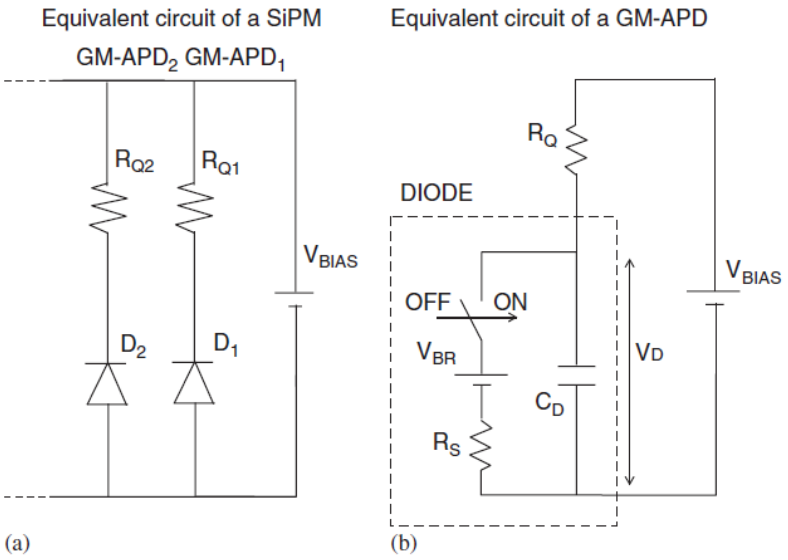

Fig. 2.12: Alternative circuit for a Silicon Photomultiplier. Figure (a) shows the circuit for the whole SiPM, while (b) shows the equivalent circuit for one pixel. ([6] fig.1.)

If a photon hits the pixel and triggers an avalanche, the circuit has to be extended by an additional resistor R_{S} (resistance of the space charge region and crystal-layers) and a voltage supply V_{Br} (breakdown voltage) (the switch is now turned on). The capacitance discharges through R_{S} and the voltage drops to V_{Br}. This results in a small current through R_{Q} until a statistical fluctuation stops it (turns off the switch again). Afterwards the capacitance starts to recharge again and the pixel becomes ready for the next photon.

Like each other detection device also a SiPM is affected by thermal noise, producing a typically very high dark counting rate, and other effects, which impair the detection efficiency of the device.

A typical pulse waveform of a SiPM is shown in the figure to the right. The signal was taken by Hamamatsu and shows a amplified SiPM waveform of one, two and three triggered pixels. It also shows one drawback of this device type. On the right side of the signal tail, after pulses are weakly indicated after some delay. Those after pulses occur due to photons reflected by the coating or by cross-talk between the different pixels. Cross-talk means that a triggered pixel also introduces an avalanche in the pixels next to it, hence one photon is counted multiple times.

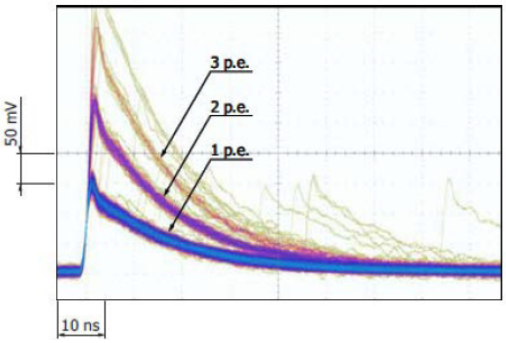

Fig. 2.13: SiPM waveform. ([11] page 2.)

If one integrates the waveforms of the SiPM (fig. 2.13), one get the characteristic peak spectrum of such a device. Those spectra are shown in figure 2.14 and 2.15 for two different mean values of impinging photons.

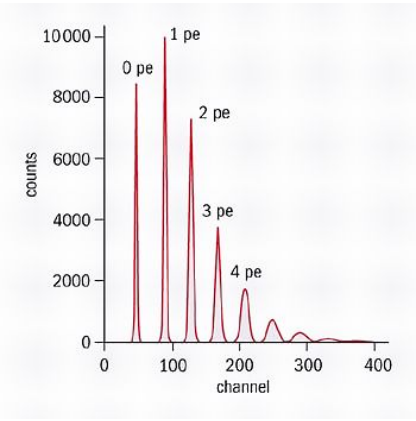

Fig. 2.14: Typical peak spectrum of a SiPM for a low illumiantion yield [15].

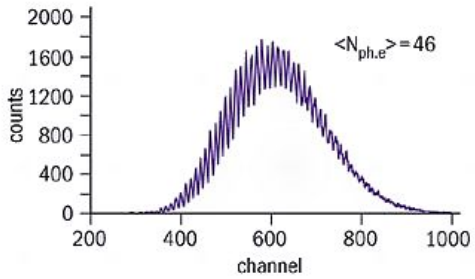

Fig. 2.15: Typical peak spectrum of a SiPM for a illumiantion yield with 46 photons in average [15].

2.4 Scintillators and LXe detectors

Scintillation media are common in many radiation detectors. Their capability to produce optical to ultra violet light that is proportional to the energy deposited by the traversing ionizing particle makes it ideal for many applications. Scintillators exist in different aggregate phases depending on the used material and experimental environment, it can be a solid, a liquid or even a gas. The most common ones are doped inorganic crystals like NaI(Ti) or ZnS(Ag) [2]. One big advantage of liquid scintillators is an easier scaling of the scintillation volume. Growing a pure crystal without defects is much harder than building a bigger vessel for liquids.

In the last 50 years detectors based on liquid noble gases had become more common. Especially xenon is a preferred scintillation medium and many applications in high energy physics, astrophysics and medical application like imaging had been developed with it. Xenon has excellent scintillation properties in addition with a high absorption power caused by the high atomic number $Z = 54$ and density $\rho = 3\,\frac{\mathrm{g}}{\mathrm{cm}^3}$. With its unique feature to generate charge carriers and scintillation photons it has a high time and energy resolution and allows to produce particle tracking detectors. This effect is just shared by liquid argon.

2.5 Scintillation in Liquid Xenon (LXe)

According to [7] the scintillation can be distinguished into two processes. Though both processes end up with an excited diatomic molecule, called excimer, which emits a 178 nm photon by de-excitation. The first process is based on the excitation of xenon atoms caused by the traversing ionizing particle or its secondaries. In our set-up we are using an ^{241}Am source (see chapter 3.1.1) to excite the LXe, the reaction can be written as

$$R + \mathrm{Xe} \rightarrow \mathrm{Xe}^* + R' \tag{2.4a}$$

$$\mathrm{Xe}^* + \mathrm{Xe} \rightarrow \mathrm{Xe}_2^{\mathrm{v}*} \tag{2.4b}$$

$$\mathrm{Xe}_2^{\mathrm{v}*} + \mathrm{Xe} \rightarrow \mathrm{Xe}_2^* + \mathrm{Xe} \tag{2.4c}$$

$$\mathrm{Xe}_2^* \rightarrow \mathrm{Xe} + \mathrm{Xe} + h\nu \tag{2.4d}$$

whereby R and R' representing the α-particle or its secondary radiation like δ-electrons and X-Ray-photons.

Formula 2.4a shows excitation of a xenon atom caused by the scatter process. Subsequently in 2.4b the exited Xe-atom forms with an other Xe-atom an excimer. The superscript v indicates additional vibration states, which can cause an emission of an infrared photon. After the relaxation in 2.4c the excimer dissociates and emits a photon by electron transitions between the lowest excited states ($^3\Sigma_u^+$ and $^1\Sigma_u^+$) and the ground state ($^1\Sigma_g^+$).
The second process starts with the ionization of a Xe-atom, also caused by a scatter with an α-particle, and can be written as:

$$R + \mathrm{Xe} \rightarrow \mathrm{Xe}^+ + e^- + R' \tag{2.5a}$$

$$\mathrm{Xe}^+ + \mathrm{Xe} + \mathrm{Xe} \rightarrow \mathrm{Xe}_2^+ + \mathrm{Xe}$$

$$e^- + \mathrm{Xe}_2^+ \rightarrow \mathrm{Xe}^{**} + \mathrm{Xe} \tag{2.5b}$$

$$\mathrm{Xe}^{**} + \mathrm{Xe} \rightarrow \mathrm{Xe}^* + \mathrm{Xe} + \mathrm{heat}$$

$$\mathrm{Xe}^* + \mathrm{Xe} + \mathrm{Xe} \rightarrow \mathrm{Xe}_2^* + \mathrm{Xe} + \mathrm{heat}$$

$$\mathrm{Xe}_2^* \rightarrow \mathrm{Xe} + \mathrm{Xe} + h\nu \tag{2.5c}$$

Following to the ionization in 2.5a the Xe^+ forms again a diatomic molecule, which is positively charged. By recombination with the emitted electron from formula 2.5a the Xe_2^+ dissociates in a higher excited Xe-atom then in 2.5b. After the recombination in 2.5b the Xe^{**} forms an excimer equally as in 2.4d under heat emission and dissociate also by the emission of a 178 nm photon. Since the normal xenon energy levels are not matching with the energy levels of the excimer the liquid xenon is transparent to the scintillation light.

For α-particles those two scintillation processes can not be distinguished and lead to the same result, but through the two different possible de-excitation transitions the light is emitted after two different decay times. Also the amount of singlet excimers and triplet excimers is not equal. Figure 2.16 shows both process schematically, while figure 2.17 shows a light signal measurement of different particles scattering in LXe.

To estimate the scintillation yield produced by an α-particle one needs to know the average required photon energy. This energy depends on the linear energy transfer of the used particle. Hence it depends on the density of produced electron and ion pairs along the trajectory of the particle. The required energy in liquid xenon for α-particles is given as [9]:

$$E_{\mathrm{ph}}^{\alpha} = 17.9\,\mathrm{eV} \tag{2.6}$$

With this value the scintillation yield can be calculated, see chapter 3.1.1.

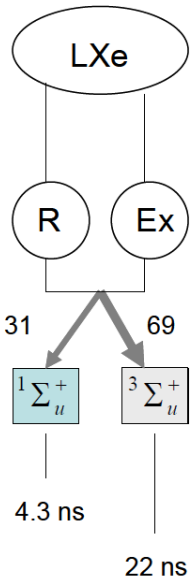

Fig. 2.16: Schematic of the LXe excitation, by recombination (R) and formation of excimer (Ex). Below the observable distributions of the singlet and triplet excimer states are shown, followed by their decay times. ([7] page 19, fig. 9)

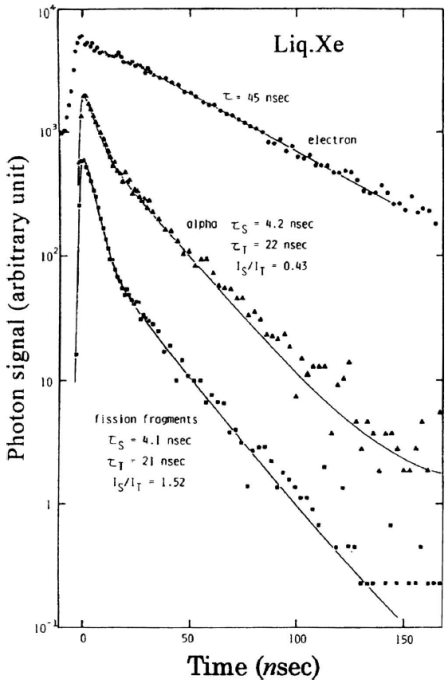

Fig. 2.17: This plot shows photon signals over the measurement time in LXe. The graph in the middle is for α-particles, it shows the signal behavior with regard to the two different decay times, as can be seen by the change of the measurement slope. ([9] page 2064, fig. 19)

3 Experimental setting and measurement set-up

In order to realize a system can be used for the characterization of SiPMs, we mainly reused an already existing setting, that were used to qualify LAAPDs as photosensors for LXe as reported in [12]. Since this characterization were done in liquid xenon as well, the core of the system could be reused like the sealed measurement vessel and the cooling infrastructure. On the other hand the existing LAAPD characterization set-up is not supporting our needed requirements, thus it will be replaced by a new one (see chapter 5). Nevertheless it will be explained in this chapter since some characteristics had been assumed, furthermore it was used for a first test-run of the setting. The so acquired data allowed us a first check of the operational readiness of the remaining setting and additional it can be treated as a first indicator for the new developed measurement set-up.

One difficulty of the realization of a test setting which is handling liquid xenon is the purity. Since impurity atoms absorb a fraction of the scintillation, a to high impurity would lead to a loss of the scintillation yield for photo sensor and the measurement would become unreproducable and incomparable with the theory. Additionally, xenon gas is not really cheap (1 kg>1000 Euro). Because of both those reasons a recirculation system becomes necessary to clean the gas continuously and recuperate it into an empty cylinder at the end.

This chapter gives a basic description of the reused setting in addition with some other important parts to understand the measurement which is explained further in chapter 4 and the development process of the new set-up in chapter 5.
Starting with an overview about the old measurement set-up and the vessel itself in section 3.1. This is followed by a description of our first SiPM from Hamamatsu Photonics and our "light" sources like a vuv LED fiber and our ^{241}Am source for the scintillation of the LXe .

In section 3.2 the cooling infrastructure for the xenon liquefaction is explained and the recirculation system, that is important for the fill in and recuperation process, is presented in section 3.3.

3.1 Measurement vessel

The core of our system is a sealed stainless steel vessel, where the xenon is condensed in order to submerge the measurement setup build inside. It has a diameter of 150 mm and a depth of 195 mm. The pressure is continuously gauged via a pressure sensor

which is important especially for the liquefaction process. For safety reasons the vessel is connected to a burst disc at the outer Dewar which will burst at an overpressure of 3.6 bar.

The vessel is thermally coupled with a copper cylinder surrounded by copper tubes for liquid nitrogen LN_2 circulation. The evaporation of LN_2 provides the necessary cooling power to condense the xenon gas inside the measurement vessel.
To measure the temperature we are using three so-called PT-100 resistors. These are resistors which change their resistance in a characteristical way if they are heated or cooled. Hence one can determine the temperature by applying a test voltage and measure the corresponding current. Thus it is advisable to get rid of the cable resistance to avoid a temperature offset. Two of them are placed inside the vessel (see figure 3.3 and 3.4) and the third one is mounted on top of the vessel (see figure 3.1).

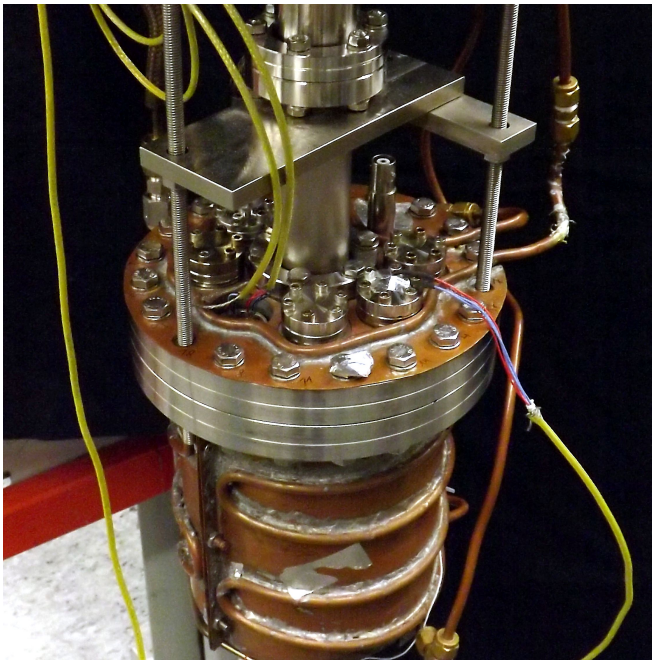

Fig. 3.1: Picture of the measurement vessel. The three yellow cables lead to a PT-100. One is fixed by a special vacuum adhesive tape on one of the small blind flanges on the topside of the vessel (cable to the right). The two other cables lead through a feed through to the PT-100 inside the vessel. Each PT-100 is soldered to four wires inside the yellow cables, enabling a 4-point probes method to avoid an offset by the cable resistance.

Inside the vessel we used the already existing LAAPD measurement set-up for our test run. It can be basically described as three disks, of which the top (T) and bottom (B) disk are mounted together by four rods (shown in fig. 3.2). The hole setup is hanging on 4 screws inside the sealed vessel. The top and middle disk and all rods are

made of stainless steel while the bottom disk machined out of Polyether ether ketone (PEEK). This material has been chosen for three main reasons:

1. Electrical isolation from the rest of the system.
2. Lower reflection coefficient than materials like stainless steel.
3. Lower outgassing than other comparable synthetics (total mass loss of 0.14% [14]).

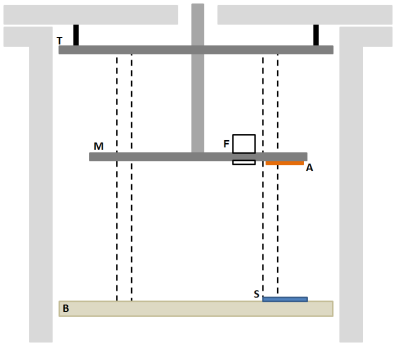

Fig. 3.2: Side view sketch of the old APD set-up. The dashed lines indicating the holding rods. They are rotated by 45° relative to the sensor. The letters represent: B bottom disk, S sensor (APD or SiPm), M middle disk, A ^{241}Am source, F fiber holder, T top disk.

In contrast to the rest of the system, the middle disk (M) is connected to a central rod that is connected to a rotary-feed-through on the top of the Dewar. This allows us to rotate the disk from the outside. This was used during the LAAPD characterization to change the position of the source, thus it was possible to characterize more than one LAAPD at the same time.

The middle disk houses an ^{241} source, fixed within specific brackets facing downwards and a polytetrafluoroethylene (PTFE) holder to fix an optical fiber. The holder guides the fiber through the disk to another stripe of PTFE. Since it is not possible to align source and fiber centrally to the detector at the same time, the stripe has the task to spread the light. This fiber can be used for sensor calibrations with LED light by emitting single photons.

In the figure 3.3 and 3.4, some stainless steel blocks can be seen between the middle and the top disks (which are not sketched in figure 3.2. This blocks are some spring holder which allows to define, in addition with some notches in the middle disk, 45°-steps during the rotation. For a further description of the spring holder, see section 5.2 on page 45 and fig. 5.8.

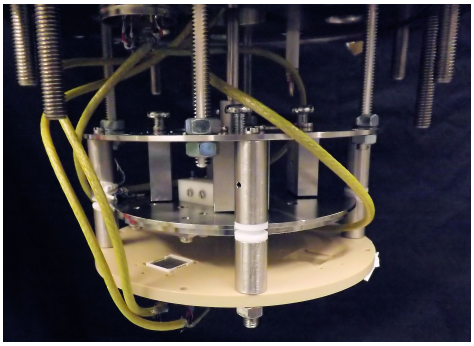

Fig. 3.3: Picture of the old measurement set-up. The white bordered device is the SiPM from Hamamatsu. The two cables on the front left side are soldered to the plugs of the SiPM in the bottom disk. The two PT-100 are connected to the other two cables.

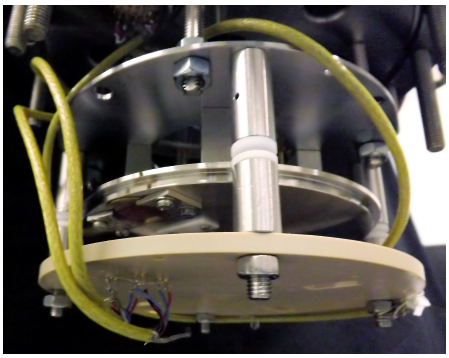

Fig. 3.4: Bottom-side view of the old measurement set-up. On the left to the middle disk is the source with its bracket holder. Behind the brackets is the spreading PTFE stripe.

In order to fix the SiPMs in plane with the surface of the PEEK disk we are reusing the APD spacers in addition with some new pins to plug in the SiPMs. This has the drawback that one is forced to solder the cables directly to the pins of bottom disk, thus the cleaning becomes a little bit difficult. The distance between source and PEEK disk, i.e. the distance between source and SiPM surface, is (18 ± 1) mm.

3.1.1 Radioactive source

The role of the ^{241}Am (Americium) source is to produce LXe scintillation light. It decays by emitting an α particle either directly into the ground state or an excited state of ^{237}Np (Neptunium). The nuclides are deposited nearby the surface of a stainless steel disk, which has a thickness of 0.5 mm and a diameter of 25 mm. The active material is concentrated within a 7 mm in the source center. The manufacturer, Isotrak lists the following specifications for the source:

Decay half time: 432.2 a

Activity(02.2008): $A_0 = (5.0 \pm 0.2)$ kBq

α-particle energy [MeV]	transition prob.[%]
5.388	1.4
5.443	12.8
5.486	85.2
others	0.6

Table 3.1: α-particle energies and their transitions probabilities.

Using the exponential decay law, the activity A_0 and the decay half time, the actual activity for the test run can be found to: activity(04.2015): $A = (4.9 \pm 0.2)\,\mathrm{kBq}$. The mean of the α-particle energy can be calculated by equation 3.1, whereby the 0.6% probability of the unstated energies has been divided uniformly to the other energies.

$$E_\alpha = \sum_{i=1}^{n} p_\mathrm{i} \cdot E_\mathrm{i} \tag{3.1}$$

$$\Delta E_\alpha = \sqrt{\sum_{i=1}^{n} p_\mathrm{i} \cdot (E_\mathrm{i} - E_\alpha)^2}$$

$$\Rightarrow E_\alpha = (5.479 \pm 0.019)\ \mathrm{MeV} \tag{3.2}$$

E_i is the α-energy from table 3.1 and the p_i the corresponding transition probability plus 0.2 for the unstated energies. If we assume a required energy of $E^\alpha_\mathrm{ph} = 17,9\,\mathrm{eV}$ (see chapter 2.5) to produce a photon by LXe scintillation, we get a mean of the total scintillation yield per decay of

$$N_\gamma = \frac{E_\alpha}{E^\alpha_\mathrm{ph}} \tag{3.3}$$

with the uncertainty given by the standard derivation of the Poisson distribution to

$$N_\gamma = 306089 \pm 553\,. \tag{3.4}$$

In order to get a better point like source, we reduce the active source diameter from $d = 7\,\mathrm{mm}$ by placing a kapton foil with a $d = 2.1\,\mathrm{mm}$ diameter hole next to the source center. The foil is thick enough to absorb all α-particles which are not emitted within the 2.1 mm. Since the source is uniformly deposited onto the steel disk the new activity can be calculated by:

$$A_{2\,\mathrm{mm}} = \frac{(2\,\mathrm{mm})^2}{(7\,\mathrm{mm})^2} A = 0.44\,\mathrm{kBq} \tag{3.5}$$

Hence the needed measurement time to achieve a respectable statistic is determined by the sampling and writing speed of the used readout electronic. Due to the fact that the counting of the α-particles is following a Poisson distribution

$$P_\lambda(k) = \frac{\lambda^k}{k!} e^{-\lambda} \tag{3.6}$$

the probability of n decays within a time range Δt can be calculated by:

$$P_{\Delta t}(n) = \frac{(A_{2\,\mathrm{mm}} \cdot \Delta t)^n}{n!} e^{-A_{2\,\mathrm{mm}} \cdot \Delta t} \tag{3.7}$$

3.1.2 LED

We have the possibility to introduce light into the vessel through the glass fiber, beside the possibility to illumined the SiPM with a radioactive source. For this purpose we use a blue LED that emits light in a range around 400 nm. The value of the wavelength is therefore not so important as long it is within in the spectral response range of the SiPM. The SiPM is a digital device, in the sense that each conversed photon leads to a complete discharge of the cell independently from the deposited energy.

Since a decay of a radioactive source occurs at random times, the advantage of a LED is to trigger the data acquisition in exactly when the light is expected. Furthermore, it is possible to define the emittance of the LED to a single photon illumination of the SiPM. Both can be done with a function generator which is giving short voltage pluses with a specific frequency.

In order to emit single photons by the LED one can use the "rule of thumb", that within 100 voltage pulses from the generator one should just detected 5 signals. This can be shown with the complementary event and the Poisson distribution (equ. (3.6)). For zero and single photons we get a probability according to the Poisson distribution of

$$P_{0.05}(0) = 0.9512$$
$$P_{0.05}(1) = 0.0476$$

thus the complementary event is given by

$$P_{0.05}(k > 1) = 1 - P_{0.05}(0) - P_{0.05}(1) = 0.0012$$

which means that only 0.12% of all events are caused by more than one photon. This can be very helpful to determine the single photon peak which is necessary for the determination of the quantum efficiency of the device.

3.1.3 Hamamatsu SiPM S10943-3186(X)/NG

Our two new silicon photomultipliers are prototypes from Hamamatsu Photonics and are especially developed for VUV light (see fig. 3.5). They had been developed in collaboration with the MEG experiment [8] and the specific details that extended the sensitivity to the VUV light has not been provided.

For the protective purpose a 0.5 mm thick quartz window is between the GM-APDs and the light source. Since quartz do not absorb VUV light and has the same reflection index ($n_{\mathrm{qu}} \approx 1.54$ and $n_{\mathrm{xe}} \approx 1.54 - 1.69$ [9]), like liquid xenon, it does not effect the photon detection efficiency. The spectral response range of the device is 130 nm to 900 nm, with a peak sensitivity wavelength of 430 nm. Both sensors have a size of (15x15) mm^2 including 4 SiPM-channels of (6.15x6.15) mm^2 which can be read out separately. Each prototype has one open side to let liquid xenon into the device. With a pixel pitch of 50 μm the total device has 60516 GM-APDs. Nevertheless, for the electrical connections between each channel and their pins the total photosensitive

area is just (5.95x5.85) mm^2 large. Hence there are some dead pixels on the outer edge of the channels.

Hamamatsu did a first function test with both silicon Photomultiplier and determined the operating voltage V_{Bias} at a gain M of $1.25 \cdot 10^6$ and the corresponding dark current I_{d} at room temperature (25 °C). Their measured values are in the subsequent table.

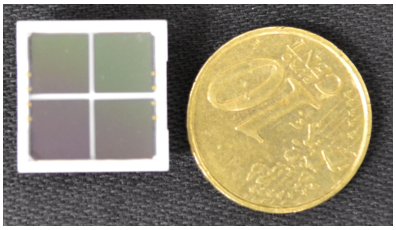

Fig. 3.5: Hamamatsu SiPM compared with a 10 Cent coin.

SiPM serial no.	channel no.	U_{Bias} [V]	I_{d} [μA]
AA00065	1	66.78	1.03
	2	66.59	4.38
	3	66.77	9.60
	4	66.69	1.69
AA00137	1	66.84	1.91
	2	66.88	1.78
	3	66.74	1.88
	4	66.83	14.25

Table 3.2: Operating voltage and dark current for $M = 1.25 \cdot 10^6$. See also appendix page 55 to 57.

Hamamatsu also gave a specification of photon detection efficiency (PDE) for each device. With a gain of $1.25 \cdot 10^6$ the PDE for light with a wavelength of 175 nm (in a evacuated environment and at 25 °C) is between 20 to 25 %. However this value should be treated with caution, because the dark count rate, like thermal noise, after pulsing and cross talk had not been taken into account. Those unwanted effects push the PDE value, thus a corrected PDE or QE value becomes more meaningful.

3.2 Cooling system

As already mentioned liquid xenon under normal conditions (standard temperature and pressure) is a gas. This is also shown in the phase diagram of figure 3.6.

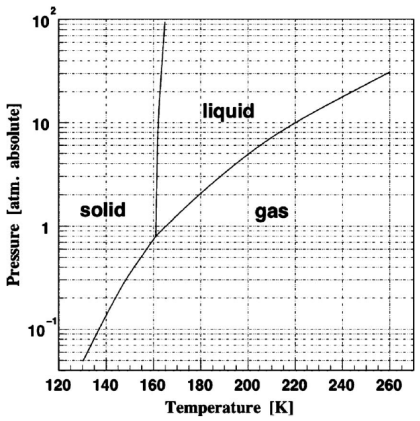

Fig. 3.6: Phase diagram of xenon. One should note that the y-axes is log-scaled. [9]

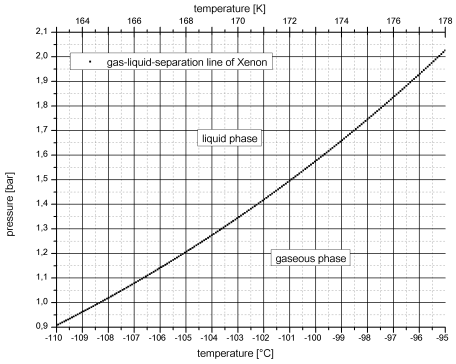

Fig. 3.7: Plotted vapor curve next to the triple point. The data had been taken from [13].

In order to use the good scintillation properties the xenon gas needs to be liquefied. Therefore we are using the evaporation of liquid nitrogen to detract energy in form of heat from the vessel and the gaseous xenon inside. The control and monitoring of the temperature can be done with the PT-100s mentioned in section 3.1. The regulation of the temperature, that means a regulation of the LN_2 flow, is done by a flow-meter that is mounted to the gas system. It measures the flow of the evaporated gaseous nitrogen in standard liters per minute. In order to avoid damaging the flow-meter one has to be sure that no liquid reaches it. Therefore we used a copper spiral right between the outlet of the supply line and the flow-meter. The flow itself can than be controlled either manually or automatically by a so-called PID-controller and the help of the PT-100's.

A **p**roportional-**i**ntegral-**d**erivative controller is an often used device for the stabilizing of different systems in science and industries. It basically tries to minimize the variance between a measured value of a sensor and the set-point value of the device. Therefore it takes "past", "present" and "future" into account by a integration of the past variances, multiplying a constant to the present variance and to derive the present variance. The advantage of this process is, that the controller just needs to know the currently measured value and nothing else about the process itself. With the summed PID-values the controller is able to control and adjust the system, like in our case the nitrogen flow and thus the temperature.

Since our final operating temperature (see. fig 3.7) is next to the triple point of xenon and also taking into account that the thermal noise of a semiconductor device

changes exponentially (equ. (2.1)), the temperature should be controlled to a stable level. This can not be achieved exclusively by the PID-controller. Hence an applied isolation vacuum and a reduction of the thermal conductivity provides on the one hand a more stable temperature and on the other hand it reduces the required LN_2 flow. For this reason the vessel is hanging inside a bigger Dewar that can be evacuated by pumping. With the rough pump we can reach a pressure of 10^{-3} mbar, in addition with a turbo molecular pump a theoretical pressure value of 10^{-9} mbar is possible. Since the hanging reduces the bearing surface and the evacuation suppresses the thermal conductivity through the air, the thermal exchange is reduced to heat radiation, thus the system becomes heat-resisting.

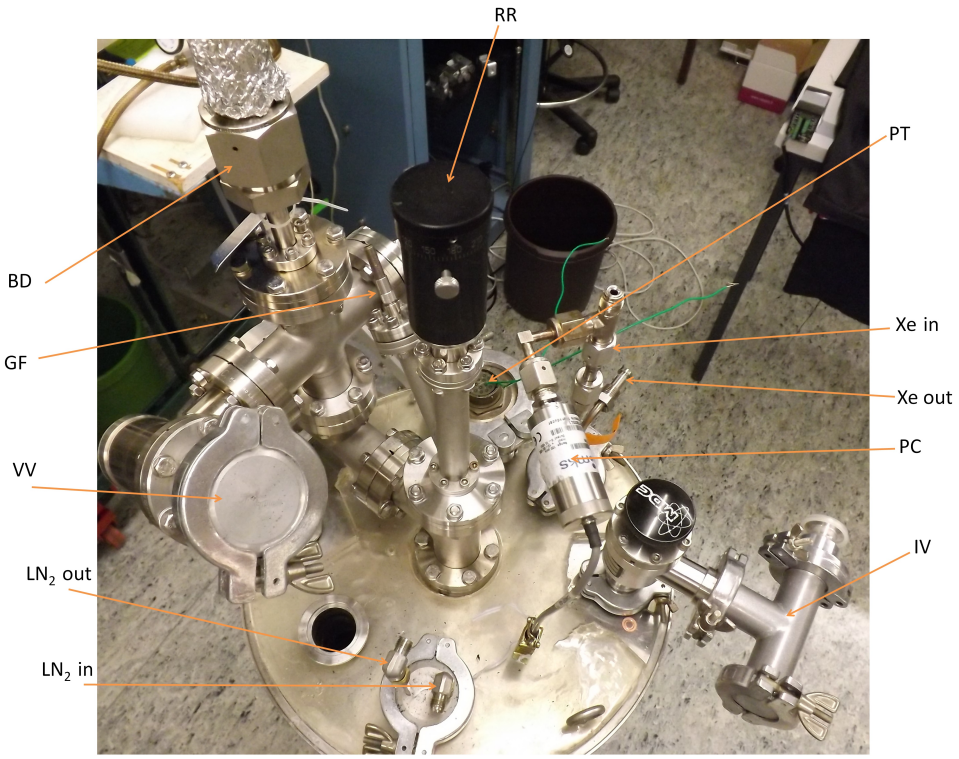

Fig. 3.8: Top view of the Dewar. The connections are: PT feed-through for the PT-100 resistors, Xe in/out xenon inlet and outlet, PC pressure sensor for the vessel/chamber, IV connection to pump the isolation vacuum in addition with a connection for a pressure sensor, LN_2 in/out nitrogen supply lines (inlet/outlet), VV connection to evacuate the vessel, GF feed-through for the glass fiber, BD burst disk (the aluminum foil is for the protection of the burst disk) and RR the feed-through and handwheel for the rotating rod.

3.3 Recirculation system

Xenon is an expensive gas, thus a closed gas system for the filling in the beginning and recuperation into the same or an empty cylinder at the end of measurement is important. Since impurities like the continuously out-gassing of the used materials, suppress the scintillation yield and make a measurement unreproducible, a continuously purification of the gas during a run becomes important as well.
In order to handle those problems we used the already existing gas system from the APD test setting. It is shown in the picture 3.9 and sketched in fig. 3.10 subsequently.

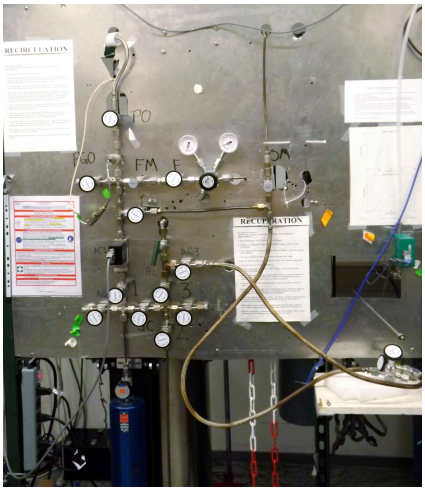

Fig. 3.9: Front side of the used gas system. All valves and devices are also sketched to the right. The getter is the dark blue cylinder in left bottom corner.

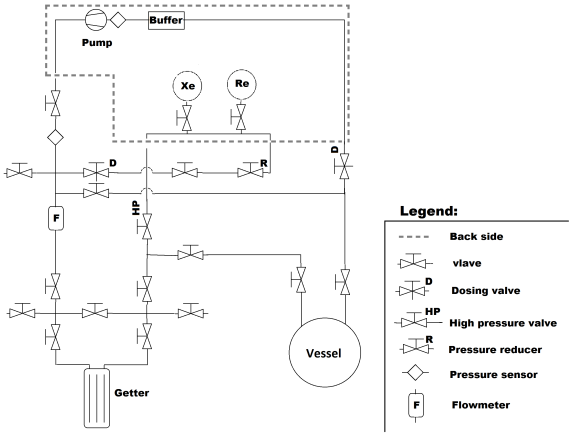

Fig. 3.10: Sketch of the gas system. The high pressure valve and pressure reducer are necessary to protect the system against the high pressure of the gas cylinders. Moreover, the pressure reducer is needed to fill the gaseous xenon from the bottle through the recirculation system into the vessel.

For the purification process we are using a so-called hot getter. The getter contains a chemical reactive material, in our case Titanoxide, that non-noble gas atoms combine with the used material by chemical reaction or absorption. In order to maximize the effect the getter material is continuously heated to apply energy in order to increases the reaction probability. To guarantee a continuous flow through the getter a small pump in addition with a buffer volume (to protect the pump for spontaneous rising pressure) is mounted on the backside of the gas system.

3.4 SiPM readout devices

The last important point of the system are the electronic devices for supply and readout of the SiPMs. For both task we made some small circuits which allow us to supply and read out each channel separately. This gives us a chance of having a cross-check between the four channels for the characterization and additionally allows us to test our set-up for electrical cross-talk of the cables and the noise of other electrical devices.

3.4.1 Voltage supply

The voltage supply is done by a typical laboratory power supply which provides us continuously 80 V d.c. voltage. It is connected to a small circuit which has mainly the task to regulate the applied voltage V_{SiPM} in a finer way then the power supply does. It is basically a voltage divider with a potentiometer to regulate the voltage. It is shown in the two subsequently figures 3.11 and 3.12. The sketch was done with the circuit simulation program *QUCS*.

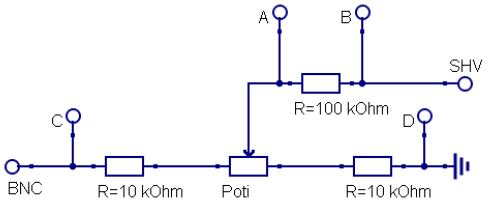

Fig. 3.11: Sketch of the supply circuit. The measurement points A and D are represented by little pin plugs in the real circuit to the right. Whereas the measurement points C and B are equivalent to the pins of the BNC and SHV connectors.

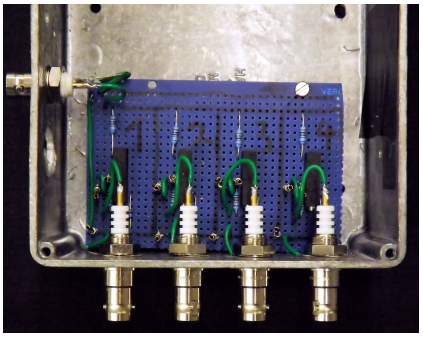

Fig. 3.12: Real supply base. It has four supply circuits as sketched to the left. Each supplied voltage can be controlled manually be screwing the potentiometer (black "box") with a small screwdriver from the SHV-connector side.

The voltage can be determined by the following equation

$$V_{\mathrm{SiPM}} = V_{\mathrm{sup}} \cdot \frac{R_2'}{R_1' + R_2'} \tag{3.8}$$

$$\text{with} \quad R_1' = R_1 + R_{\mathrm{P}} \quad \text{and} \quad R_2' = \frac{R_2 \cdot (R_3 + R_{\mathrm{L}})}{R_2 + R_3 + R_{\mathrm{L}}}$$

and depends on the values of the resistors $R_1 = 2\,\text{kOhm}$, $R_2 = 10\,\text{kOhm}$, $R_3 = 100\,\text{kOhm}$, R_P and R_L, where R_P is the changeable resistance of the potentiometer and R_L is the resistor load of the further circuit. This allows a voltage range of 36.00 V to 76.00 V in steps of 0.01 mV.
This device is a preliminary solution for the first test measurement, due to the short time constrained of my thesis.

3.4.2 Data acquisition (DAQ)

For the read-out a small circuit was manufactured including a low-pass filter between the power supply and the SiPM and a capacitance in addition with a small resistor in parallel after it. Thus with the filter we get rid of high-frequent noises caused by the power supply and other electronics.

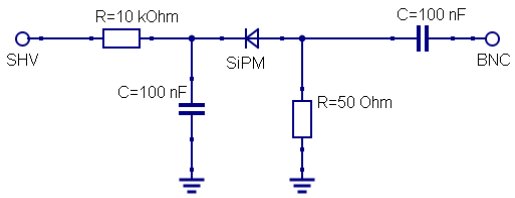

Fig. 3.13: Sketch of the read-out circuit. The SiPM is represented by the reverse-biased diode. The SHV side is connected to the SHV-plug of the voltage divider. The BNC connection goes on the other to the oscilloscope for the data acquisition.

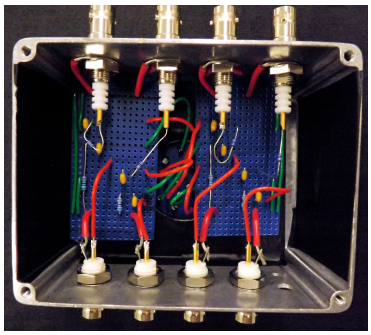

Fig. 3.14: Real base with all four read out circuits. Each channel can be read out separately.

With the values stated in the sketch fig. 3.13 the filtered frequencies of an ideal

low-pass filter can be found with

$$
\begin{aligned}
I &= \frac{V_{\text{in}}}{|Z|} \\
\Rightarrow V_{\text{out}} &= \frac{|X_{\text{c}}|}{|Z|} \cdot V_{\text{in}} \\
\Leftrightarrow V_{\text{out}} &= \frac{1}{\sqrt{1 + (\omega \cdot C \cdot R)^2}} \cdot V_{\text{in}}
\end{aligned}
$$

together with the criterion of the cut-off frequency $V_{\text{in}} = \frac{V_{\text{out}}}{\sqrt{2}}$ to

$$
\begin{aligned}
\Rightarrow \sqrt{2} &= \sqrt{1 + (\omega \cdot C \cdot R)^2} \\
\Rightarrow f_{\text{c}} &= \frac{1}{2\pi \cdot C \cdot R} \approx 159\,\text{Hz}
\end{aligned} \tag{3.9}
$$

and higher. Hence we ensure that most of the high frequent noises are filtered out and the signal is not effected by it.

For the signal decoupling we using a 100 nF capacitor in addition with a 50 Ohm resistor. This has the advantage that we get rid of any left over DC voltage that could cause an offset of the signal. Additionally it translate the current signal of the SiPM into a voltage signal that can be read out with an oscilloscope. The small resistor ensures a fast de-charge of the capacitor to return to the starting conditions.
The possibility to amplify the voltage signal has been discarded, since the available amplifiers could not bring any advantage because of two reasons:

1. They could be placed only outside the Dewar, which means that also the noise would have been amplified.

2. The signal was already large enough to be detected without any amplification.

For the data acquisition itself we are using an oscilloscope from *Agilent Technologies* of the infiniium 9000 series. It is a *DSO 9254A* model and has the following specifications:

Analog bandwidth.	Analog sample rate 4-channel/2-channel	Standard memory 4-channel/2-channel	Scope channels	vertical resolution
2.5 GHz	10 GSa/s / 20 GSa/s	20 Mpts/40 Mpts	4	8 Bit

Table 3.3: Specifications of the DAQ oscilloscope. [16]

4 Initial measurement with the existing set-up

The first measurement at the end of my thesis was an important step to establish the test setting. The primary goal was the development of a method to determine the photo detection efficiency as explained in section 4.1. Therefore it is necessary to determine the effective illumination yield of the source or the LED on the SiPM. This can be done analytically or with a simulation as described in section 4.2. At the end of this chapter will be a short representation of the first result in liquid xenon in addition with a briefly discussion (section 4.3).

The initial run started after 18 days of recirculation of a small amount of xenon through the getter and was done from Tuesday the 26. until Friday the 29. of June. In order to give a brief overlook of the measurement, it will be described in the following.

In the first day and night we measured the behave of the SiPM (serial no. AA00137) for different voltages in gaseous xenon. The pressure inside the vessel was 2.553 bar at a temperature of $\sim 220\,\mathrm{K}$.

From Wednesday until Thursday evening we continued the cool down of the vessel until we reached a temperature of 178 K, then we started the filling process. For our initial test-run we needed 3.87 kg of xenon inside the vessel to have source and SiPM in liquid. In order to be ensure we put 3.95 kg which had been integrated by the data of the flow-meter.

After the liquid xenon had been deposit into the vessel we tried to stable the system with the PID controller until a reproducible measurement was possible. At a temperature of 166 K we measured in a voltage range of V_{bias} from 58 V in 0.5 V steps until 60.5 V. The specific settings of the oscilloscope during the data acquisition are shown in figure 7.6 which is attached to the appendix on page 58. For each voltage set-point we measured 10 k or 20 k waveforms of the illumination from the scintillation or of a single photon illumination with the LED.

4.1 Photon detection efficiency and analysis approach

The Photon Detection Efficiency (PDE), as already written in the theory foundations can be seen as a ratio

$$\mathrm{PDE}(\lambda) = \frac{\#\text{generated current pulses}}{\#\text{impinging photons}(\lambda)} \tag{4.1}$$

and is the most important quantity of a photon detection device. Especially for solid state detectors, it can be rewritten as

$$\mathrm{PDE}(\lambda) = \mathrm{QE}(\lambda) \cdot F \cdot \epsilon \tag{4.2}$$

with the so-called fill factor F which is a ratio between active and passive area of the sensor, the avalanche trigger probability ϵ and the quantum efficiency QE. Whereby the quantum efficiency can be written as

$$\mathrm{QE} = \frac{\#\text{converted photons}}{\#\text{impinging photons within the active area}} = \frac{N_{\mathrm{eh}}}{N_{\mathrm{im}} \cdot F} \tag{4.3}$$

$$\Rightarrow \mathrm{PDE} = \frac{N_{\mathrm{eh}}}{N_{\mathrm{im}}} \cdot \epsilon \tag{4.4}$$

The fill factor F is a quantity that depends by the geometry of the GM-APD cell and it is generally provided by the supplier. For the impinging photons N_{im} we need to calculate the illumination yield which can be done analytically or with a simulation and is going to be explained in the following section. Hence the goal of our current and especially of our new measurement set-up is to determine the generated electron-hole pairs $N_{\mathrm{eh}} \cdot \epsilon$ in form of the integrated charge from the oscilloscope voltage signal. That means we have to rewrite equation (4.4) into

$$\mathrm{PDE} = \frac{Q}{e \cdot M} \cdot \frac{1}{N_{\mathrm{im}}} \tag{4.5}$$

with the gain M and the elementary charge e. Since our measured signal is a voltage signal V_{sig} over time we have to calculated at the first order of approximation the charge carriers Q by

$$Q = \int_{t_0}^{t_0+\Delta t} \frac{V_{\mathrm{sig}}(t)}{|X_{\mathrm{c}}|}\,\mathrm{dt} \tag{4.6}$$

with the impedance of the decoupling capacitor X_c and the signal length Δt. Since we have to estimate the impedance of the capacitor and furthermore we do not know the gain M of our device for our measurement set-points, we have to by pass this difficulty.

Therefore we can exploit the nature of the SiPM, that each measured photon leads to the same current. Hence if we can determine the integrate voltage V_{i} of a single photon $V_{\mathrm{i}}^{\mathrm{single}}$ by

$$V_{\mathrm{i}}^{\mathrm{single}} = \int_{t_0}^{t_0+\Delta t} V_{\mathrm{sig}}^{\mathrm{single}}(t)\,\mathrm{dt} \quad , \tag{4.7}$$

we can easily determine $N_{\mathrm{eh}} \cdot \epsilon$ by

$$N_{\mathrm{eh}} \cdot \epsilon = \frac{V_{\mathrm{i}}}{V_{\mathrm{i}}^{\mathrm{single}}} \quad . \tag{4.8}$$

Hence the photo detection efficiency can be found to

$$\mathrm{PDE} = \frac{V_\mathrm{i}}{V_\mathrm{i}^\mathrm{single}} \cdot \frac{1}{N_\mathrm{im}} \tag{4.9}$$

which can be calculated with the illumination yield N_im determined by the simulation in the next section 4.2 and the peak spectrum of the LED to determine $V_\mathrm{i}^\mathrm{single}$.

4.2 Calculation and simulation of the effective illumination

Based on the theory and the previous chapter, the characterization of the SiPMs, e.g. determining their quantum efficiency and thus the photon detection efficiency, it is necessary to change the illumination yield in a controllable and reproduceable way. Since a radioactive source emits its particles isotropically, the easiest way to calculate and change the illumination yield is the so-called solid angle. It can be seen as an equivalent to a normal angle in two dimensions and is given by the ratio between a subsurface and the total surface of a sphere.

Under the assumption of a point like source the solid angle can be approximated as the ratio between the SiPM active area and a sphere with the distance between source and SiPM as radius. Hence the solid angle can be written as

$$\Omega(r) = \frac{\mathrm{a}}{4\pi \cdot r^2} \tag{4.10}$$

with a being the active area of SiPM. Nevertheless this is a approximation and not necessarily valid for low heights like 20 mm (as a reminder: the total area of the SiPM is $(15\,\mathrm{x}\,15)\,\mathrm{mm}^2$), since one has to deal with the projection of the SiPM surface to a spherical surface. Since the SiPM prototype from Hamamatsu has 4 channels, which are all displaced from the center of the device, this projection can be very complicated. Thus we tried another approximation and will compare it later with the results from a simulation which is dealing with the illumination yield as well.

In order to calculate the illumination yield analytically, at first we took the ratio between the active area and the passive illuminated area. This ratio is not equal to the fill factor F as shown in the following figure 4.1.

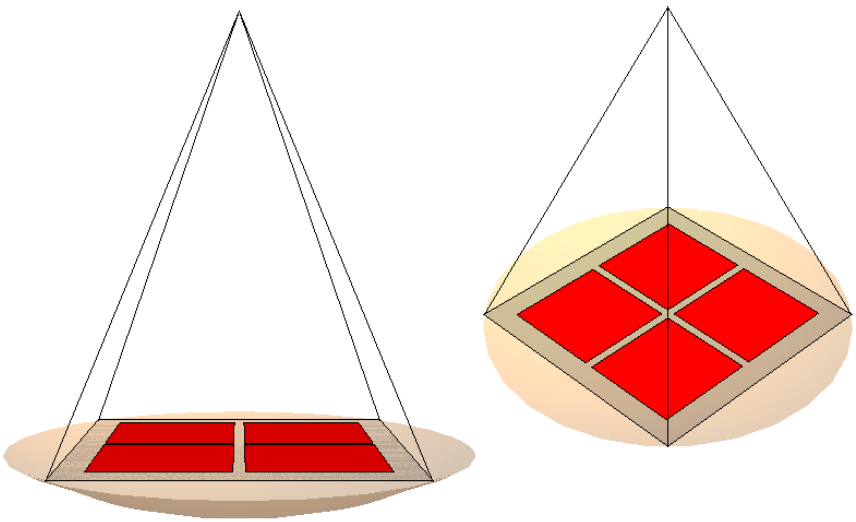

Fig. 4.1: Sketch of the Hamamatsu SiPM under the illumination of a point like source in 20 mm height (tip of the pyramid). Grey is the passive area of the SiPM red the four active areas (channels). Furthermore is shown in the left scheme the subsurface of sphere which belongs to the projection of illuminated circle in the right sketch.

In order to calculate the projection of the active area to the spherical surface we assumed that the passive and active area (see fig. 4.2 to the right) is projected in linear way, that we can calculate the new active area by

$$\begin{aligned} \text{active area subsphere} &= \frac{\text{active area SiPM}}{\text{whole area circle}} \cdot \text{subsurface sphere} \\ \Leftrightarrow a_{\text{asubs}} &= \frac{a}{a_{\text{c}}} \cdot a_{\text{subs}} \end{aligned} \tag{4.11}$$

where the area of the subsurface of the sphere is given by

$$a_{\text{subs}} = \int_0^{2\pi} \mathrm{d}\phi \int_{\pi-\alpha}^{\pi} R^2 \cdot \sin(\theta)\, \mathrm{d}\theta \quad . \tag{4.12}$$

Together with

$$\begin{aligned} R(h) &= \sqrt{d^2 + h^2} \quad \text{with} \quad d = \sqrt{2 \cdot 7.5^2}\,\text{mm} \\ \alpha(h) &= \arctan\left(\frac{d}{h}\right) \end{aligned}$$

the integral only depends on the distance h between SiPM and source and the half side with of the SiPM (7.5 mm). With the mean value of photons, that are produced by our α-source, N_γ and the height difference of the already existing set-up given in the

previous chapter (h=18 mm), we can determine the illumination yield of the active area of one channel. It should be mentioned additionally that we assumed the active area to be $(6.4\,\mathrm{x}\,6.4)\,\mathrm{mm}^2$ including the dead pixels. Hence we get according to (4.11) a illumination yield of

$$N_{\mathrm{illu}} = \frac{a_{\mathrm{asubs}}}{4 \cdot 4\pi R^2} \cdot N_\gamma = 2456 \;\; \text{Photons.} \tag{4.13}$$

At the end of this section we are going to compare this value with the simulated one.

The used simulation program for the illumination yield was written in *C++* provided by the group and includes the main idea to change the solid angle by height. In addition, the simulation supports different collimator types and a number of collimators which is important during the development process of the new set-up. The working principle and the main results will be shown here, whereas special results, like for the collimators are shown later.

The simulation is basically a repetition of If-loops which check if an isotropic, emitted photon impinges on the sensor surface or not. Therefore we need at first the simulation of an isotropic source. This can be achieved with spherical coordinates or Cartesian coordinates, we chose later according to [10]. In order to distribute events equally over the surface of a unity sphere, one picks the coordinates $(x', y', z')^T$ Gauss distributed:

$$N(\mu = 0, \sigma^2 = 1) = \frac{1}{\sqrt{2\pi}} \cdot e^{-\frac{x^2}{2}} \tag{4.14}$$

By a normalizing of $(x', y', z')^T$ according to

$$\frac{1}{\sqrt{(x'^2 + y'^2 + z'^2}} \cdot \begin{pmatrix} x' \\ y' \\ z' \end{pmatrix} = \begin{pmatrix} x \\ y \\ z \end{pmatrix}_{\mathrm{Norm}} \tag{4.15}$$

one gets uniformly distributed points on the unity sphere. In this context the mean μ has to be 0, whereas the variance σ^2 can be chosen freely. The result of this method is shown in the subsequent figure 4.2 to the left.

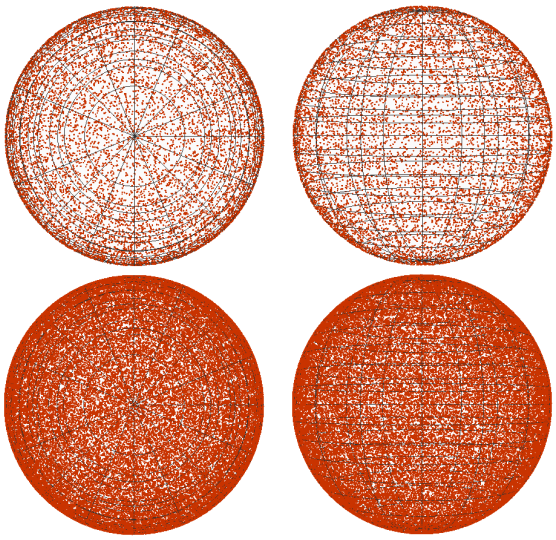

Fig. 4.2: Uniformly distributed events over the sphere surface according to [10]. The top row shows top and side view with 10 k points, in contrast to the bottom row with row 50 k events.

Those generated event coordinates d (for direction) can be used, together with a starting point s (e.g. source) and a parameter t(h), to from an equation of a line which can be used to determine the illumination path of the photons for the If-loop.

$$g : \begin{pmatrix} s_\mathrm{x} \\ s_\mathrm{y} \\ s_\mathrm{z} = 0 \end{pmatrix} + t(h) \cdot \begin{pmatrix} d_\mathrm{x} \\ d_\mathrm{y} \\ d_\mathrm{z} \end{pmatrix} \quad (4.16)$$

To save cpu time, all photons should be emitted in the hemisphere of the sensor ($\Rightarrow d_\mathrm{z} = |d_\mathrm{z}|$). Taking into account that the source is not a point-like source with an openeing diameter of 2.1 mm, the starting points s are uniformly distributed under the term to compensate this:

$$1.05 \geq \sqrt{s_\mathrm{x}^2 + s_\mathrm{y}^2} \quad (4.17)$$

The parameter $t(h)$ is a scaling parameter which depends on the distance between the source and the next collimator or the sensor surface. It has to be recalculated for each collimator and is given by:

$$t(h) = \frac{h_\mathrm{i}}{d_\mathrm{z}} \quad (4.18)$$

With equation 4.16 and 4.18 one can determine the x and y coordinates in the plane defined by h_i, hence one can ask with an If-loops, if the particle goes through the collimator opening or not. The collimators differ in 2 types of holes and 2 different hole positions. The two hole types are round holes with the radius as parameter and squared holes with half the side length as parameter. The position can be in the center, or as a quad-holed collimator with an equidistant in x and y direction. They are sketched in the following figure 4.3.

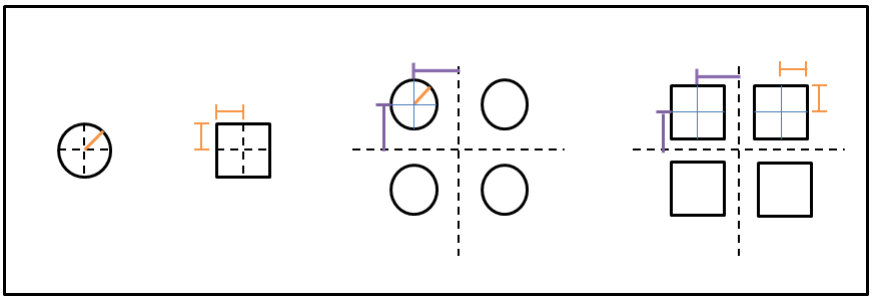

Fig. 4.3: Sketch of the four collimator types. The dashed cross shows the position of the collimator $(0, 0, h_i)^T$, whereas the colored lines show the two parameter of the collimator: orange for the opening size and purple for the hole displacement.

All photons which passed all collimators are filled in a two-dimensional histogram, that has a range equal to the size of SiPM and a bin size equal to the pixel pitch. Bins which representing passive area had not been filled at all.

The final program structure of the simulation can be sketched like in figure 4.4. The boxes stand for a logical question in the program code. The response and the progress is shown with the colored lines, green means true and red false.

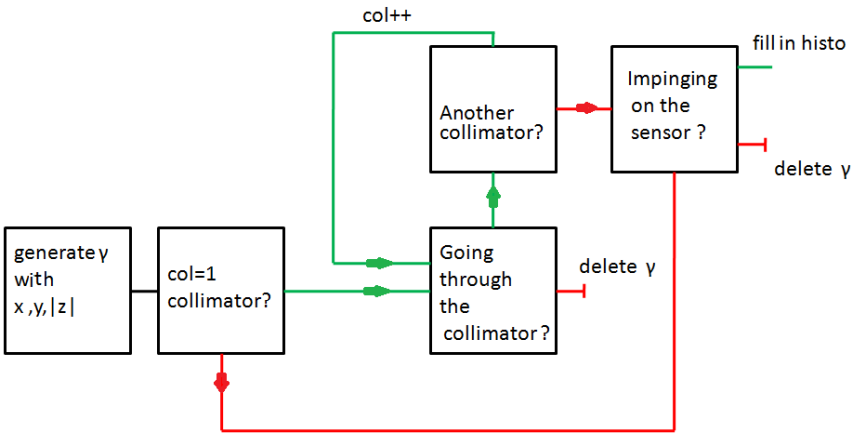

Fig. 4.4: Sketch of the simulation. Green means true and red false as response.

Subsequently are shown as example the results of a simulation of the already existing set-up, which was explained in section 3.1. As a reminder: the source is covered with a Kapton foil with an opening of 2.1 mm in diameter and has a total height difference of 18 mm to the SiPM. The mean number photons N_γ has been taken from equation (3.4). Taking into account that the number of photons are Poisson distributed in addition to the fact that $N_\gamma \gg 10$, we can use a Gaussian distribution with $\mu = N_\gamma$ and $\sigma^2 = \sqrt{N_\gamma}$ as an approximation to generate a pseudo-random number of photons.

In order to achieve good statistics all simulations were carried out with 100 k α-

decays, which means 100 k times around 306089 events (photons). Fig. 4.5 and 4.6 showing two-dimensional histograms which are representing the Hamamatsu SiPM active surface. They are filled with an overall events integrated and normalized distribution of impinging photons for two different PDE values. Whereby the PDE is taken into account by "rolling a dice" for a 30% probability. Each histogram bin is representing a GM-APD with its position in x [mm] and y [mm] equivalent to the device. The white cross in the middle represents the passive spacer between the four channels and the bin contents had been set there to 0. The dead pixels at the edges of the device have not been taken into account.

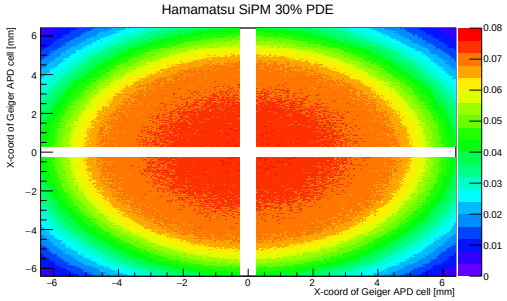

Fig. 4.5: Distribution of the illumination yield with a 30% PDE

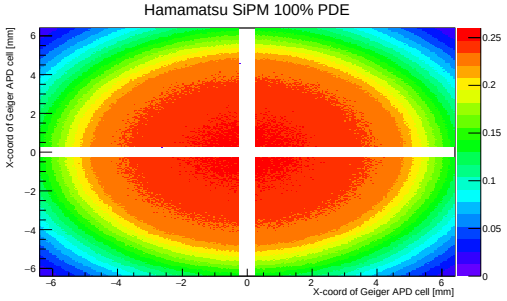

Fig. 4.6: Distribution of the illumination yield with a 100% PDE

If we put the summed number of all detected photons of all 100 k decays into a one-dimensional histogram we can determine the mean value of the expected scintillation yield. Furthermore with the simulation we can take into account that multiple cell hits are detected as one photon and can distinguish between detected photons and impinging photons. This is shown subsequently in figure 4.7 for one of the four channels.

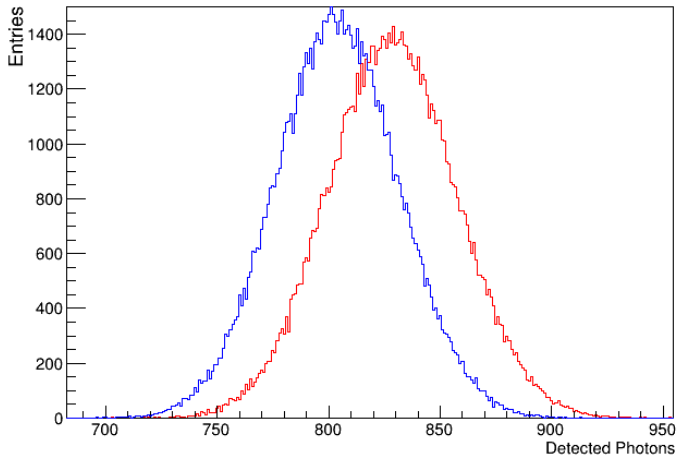

Fig. 4.7: Histogram of the sum of all detected photons over all 100 k decays for one channel. The detected photons are represented as blue curve (multiple hits of a cell are counted as one) whereas the impinging photons are represented by red curve.

If we approximate again the Poisson distribution by a Gauss distribution and fit both peaks (see Appendix page 59 figure 7.7) we get the following fit values:

FIT	N_0	μ	σ
Detected Photons	1449 ± 6	803.9 ± 0.1	27.5 ± 0.1
Impinging Photons	1387 ± 5	828.6 ± 0.1	29.7 ± 0.1

Table 4.1: Fit values of the detected and impinging photon peaks of the already existing set-up.

If we take the analytic value from equation (4.13) and rescale it with the 30% PDE we can compare it with the simulated value from the table 4.1

$$N_{\text{ana}} = 0.3 \cdot N_{\text{illu}} = 737 \quad N_{\text{sim}} = \mu_{\text{imp}} = 826 \tag{4.19}$$

and get a relative uncertainty of

$$\frac{N_{\text{ana}} - N_{\text{sim}}}{N_{\text{sim}}} \approx -0.121 \quad . \tag{4.20}$$

This 12% uncertainty shows, that we can roughly estimate the illumination yield analytically. Though is the simulated value with its good statistics of 100 k α-decays the better choice to give a expectation for the measurement.

4.3 Preliminary of the initial results in liquid xenon

The analysis of the data from first test-run has just started and is still on going. The first goal was to determine the PDE and the gain, but due to the short time constraints of my thesis we could not finish the analysis. Hence this section will give a first indication and a brief overlook of the data so far.
We have chosen two data-sets of the LED and source of the highest voltage set-point ($V_{\text{bias}} = 60\,\text{V}$, $V_{\text{bias}} = 60.5\,\text{V}$).

At first we want to present the data-sets of the blue LED, because they are crucial to determine the photo detection efficiency of the SiPM, as already shown in section 4.1. Both sets had been taken by a temperature of 166 K and including 10 k (for $V_{\text{bias}} = 60\,\text{V}$) and 20 k (for $V_{\text{bias}} = 60.5\,\text{V}$) waveforms. As example are shown subsequently in figure 4.8 two waveforms which were detected by channel one.

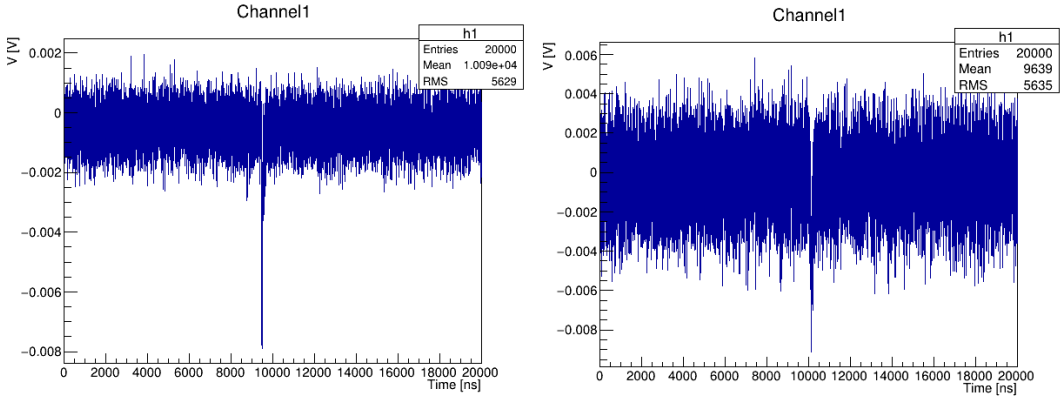

Fig. 4.8: Two recorded waveforms during the illumination of the LED. Both waveforms had been detected with the same channel of the SiPM. The left waveform was measured by $V_{\text{bias}} = 60\,\text{V}$ and the right one by $V_{\text{bias}} = 60.5\,\text{V}$.

In order to determine the integrated voltage of the single photon peak $V_{\text{i}}^{\text{single}}$ we integrated all waveforms of channel one within the range of the LED signal (9420 ns to 9740 ns for $V_{\text{bias}} = 60\,\text{V}$ and 10000 ns to 10400 ns for $V_{\text{bias}} = 60.5\,\text{V}$) and put those values into a one-dimension histogram to acquire a peak spectrum from the LED. The spectra for both voltages are shown in the following figure 4.9. It should be mentioned, that both plots still need to be corrected concerning an offset from the baseline.

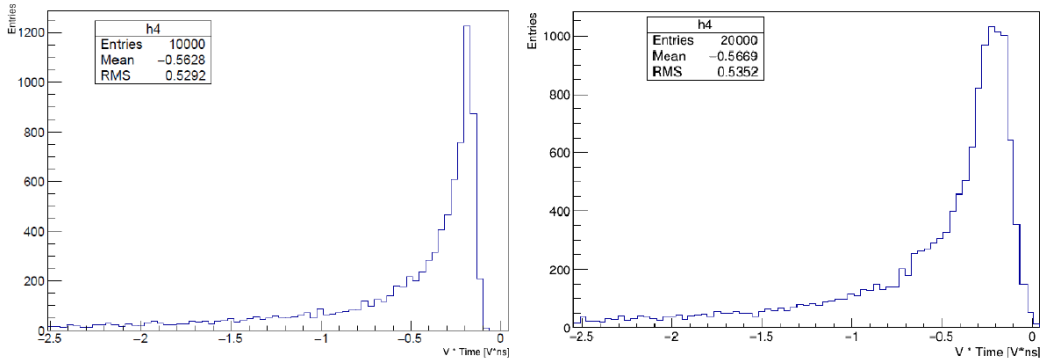

Fig. 4.9: Spectra of the blue LED. The left plot shows the spectrum for $V_{\text{bias}} = 60\,\text{V}$ and right one for $V_{\text{bias}} = 60.5\,\text{V}$. The identification of the different (0,1,2,...) photon peaks is not possible.

It seems that the characteristic photon peaks of the SiPM are broad enough to overlap each over, due to the fact of this we can just identify the blurred resulting Poisson distribution. Thus the typical photo spectrum like shown in fig 2.14 on page 11 can not be seen. That the 0 photon peak is slightly shift to a bin value of $\sim 0.25\,\text{V}\cdot\text{ns}$ is caused by the baseline.

The results of the source seem to be similar to the results of the LED. Their spectra are shown in fig. 4.12. It is also not possible to identify a clear peak spectrum like shown in fig. 2.15 on page 11. To acquire the peak spectra of the source we used the same approach and integrated all waveforms of the corresponding data-set within in a range of 14490 ns to 15400 ns. Two of the waveforms are shown as an example in figure 4.10. The waveform of $V_{\text{bias}} = 60\,\text{V}$ (fig. 4.10 to the left) shows additionally a potential single dark count which is bigger plotted in figure 4.11.

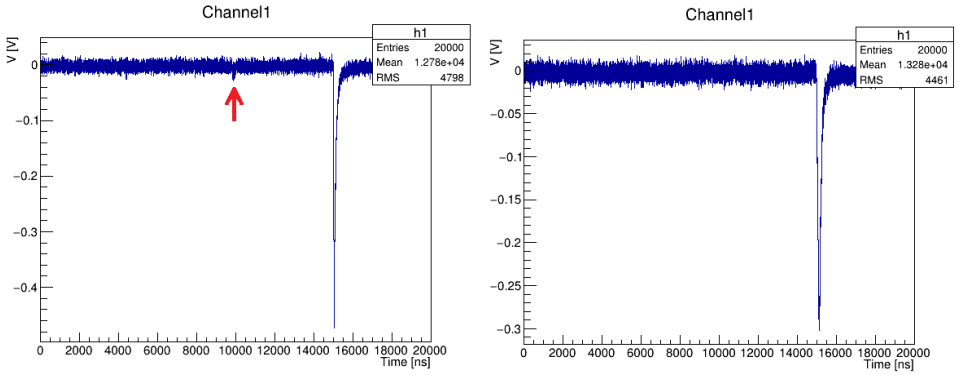

Fig. 4.10: Two recorded waveforms during the illumination of the source. Both waveforms had been detected with the same channel of the SiPM. The left waveform was measured by $V_{\text{bias}} = 60\,\text{V}$ and the right one by $V_{\text{bias}} = 60.5\,\text{V}$. Furthermore indicates the red arrow a potential single dark count.

The first run over the measured data indicates that the current of dark counts like shown in figure 4.11 is pretty low. Though as shown, could the analysis of it become a difficulty since they are in the same order of magnitude as our noise. In order to determine the dark current, rather than estimate it by a quick look, we have to write a peak finder which can handle this job.

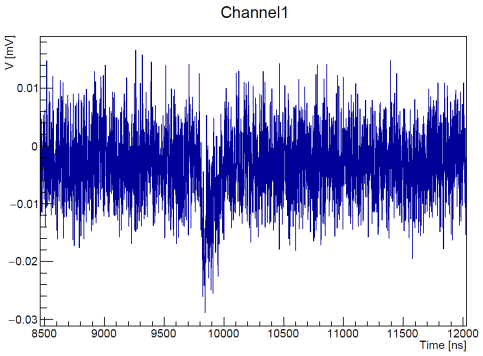

Fig. 4.11: Plot of the zoomed dark count from figure 4.10.

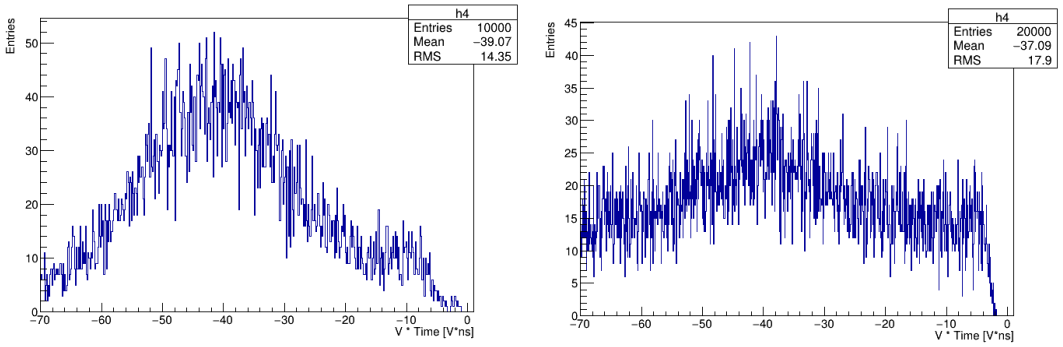

Fig. 4.12: Putative peak spectra of the source. The left plot shows the spectrum for $V_{\text{bias}} = 60\,\text{V}$ and right one for $V_{\text{bias}} = 60.5\,\text{V}$. A clear identification of a peak structure is not possible.

In order to determine correlations between the three measured channels we filled different two-dimensional histograms with the integrated voltages of their waveform. A comparison between them allows us to cross-check the channels if they have a different behavior e.g. a different avalanche trigger probability ϵ (see equation (4.4)).

The correlation of the channels for the chosen data set-points are shown in figure 4.13. It seems that no one of the three channels do have a special behavior which does not fit to the other two. The correlation plots of $V_{\text{bias}} = 60.5\,\text{V}$ (fig. 4.13 second row), indicates further the formation of two cluster structures at (-40 V ns, -40 V ns) and (-70 V ns, -70 V ns).

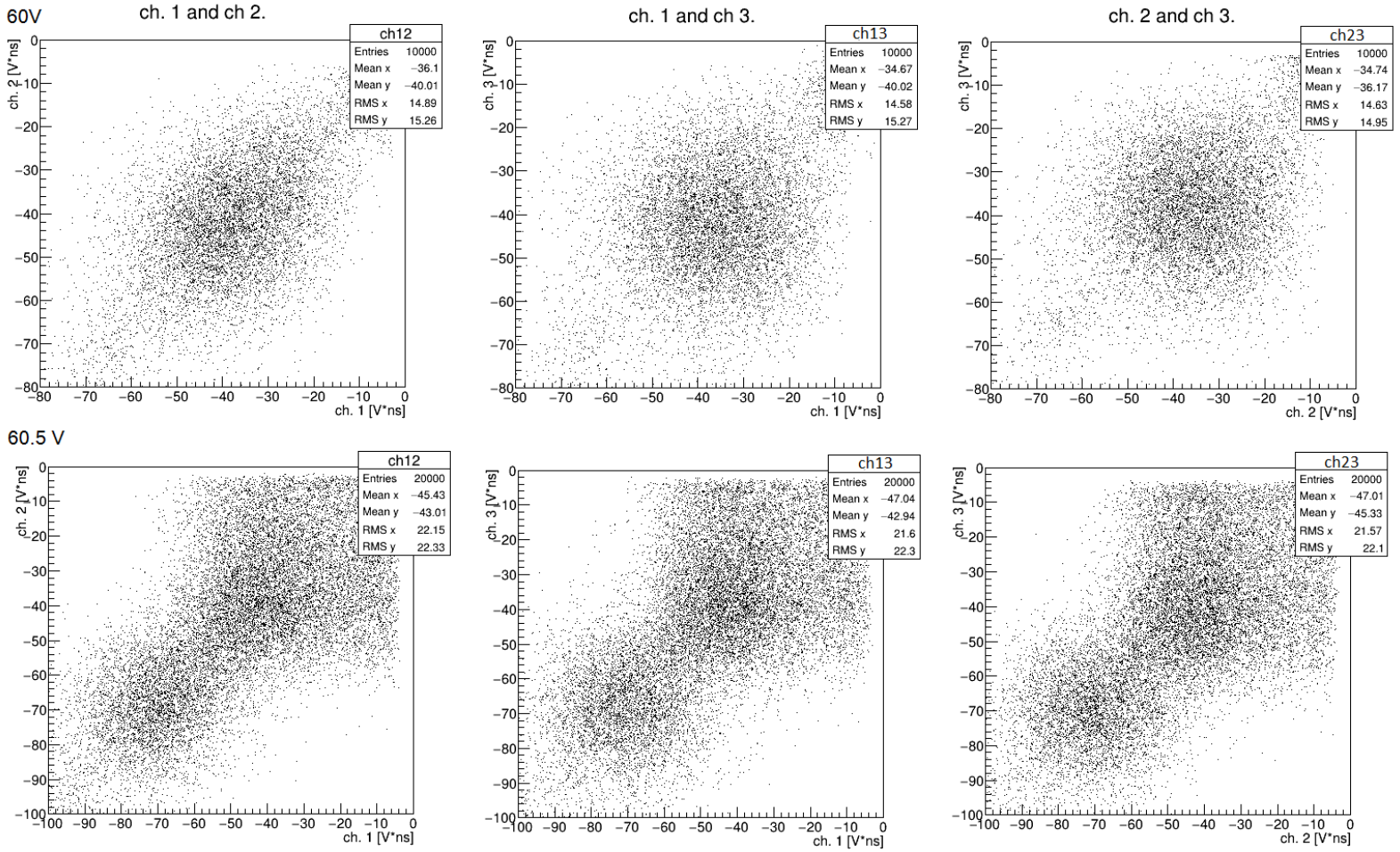

Fig. 4.13: Correlation plots of the three different channels of the SiPM. The first row shows the correlation of the $V_{\text{bias}} = 60\,\text{V}$ data, whereas the second row shows the $V_{\text{bias}} = 60.5\,\text{V}$ data. Furthermore indicates the second row the formation of two clusters at (-40 V ns, -40 V ns) and (-70 V ns, -70 V ns).

4.4 Discussion on the preliminary results

As mentioned in the previous section, the analysis of the data has just started. Though this preliminary look over the data indicates that it might be not possible to determine the single photon peak neither from the LED nor the dark count. Since the analysis approach was based on it, any further determination of the PDE was not possible. In addition we are not able to compare the results from the measurement with the simulation, because we are not able to determine the number of detected photons. Thus a further characterization such as determining the gain, the dark count rate, cross talk or after pulsing is not possible.

The main issue was the blurring of the single photon peak within the electrical noise as shown in figure 4.14. The noise seems to be in the same order of magnitude as a potential single photon peak.

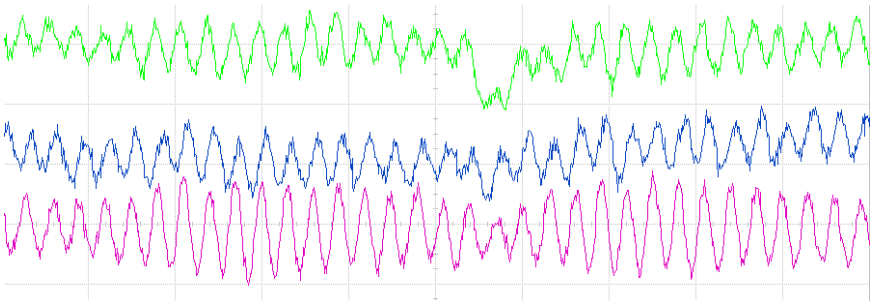

Fig. 4.14: "Screen shot" of the oscilloscope. The waveforms showing the noise rate of the three SiPM channels. Additional was a potential single dark count recorded within the green waveform. The vertical axis is in 1 mV/div and the horizontal axis in 100 ns/div.

5 Design and studies of a specific set-up for SiPMs

This chapter will give an introduction and explanation of the new measurement set-up, which is especially designed for the characterization of SiPMs. It should provide an easier measurement of the photon detection efficiency, due to the fact that the illumination yield is changeable.

It had taken a big part during my thesis and three set-ups have been developed, which differ in improvements and also introduce new features, considered during the development process and the initial test run.

The main structure is linked to the simulations which provide the information about the required specifications, whereas the vessel constrains the actual dimensions of the set-up. Basically, it is a change from the old rotatable into a new liftable set-up to take data for different solid angles. This can be achieved by using the pitch of a thread, allowing to have a slope of 1 mm per rotation (standard metric thread). The total possible height difference is then determined by the vessel dimensions, disk sizes and some spacers for the cable bending. All designs were done with the CAD program *SolidWorks*.

The explanation of the new measurement set-up will be divided into two sections. The following section 5.1 will deal with the first version of this new measurement set-up, due to the fact that it explains the basic ideas. Additional it showed some issues whose solutions lead us to the final version, that is going to be explained in section 5.2.

5.1 Variable source-sensor distance set-up, a first attempt:

In comparison to the previous measurement set-up, some minor changes for the new design were applied. At first, the connection between middle disk and the rotating rod was replaced by a threaded hole in addition with a new threaded rotating rod to get a liftable middle disk. To be able to change the height by "screwing" the middle rod, it is essential to prevent the middle disk from rotating. Therefore the diameter was set to the same one as for the other disks. In addition, with four holes it is possible to use the outer rods to guide the middle disk in height and fix it in the plane. For a sliding improvement all four rods had been coated with PTFE tubes. The source and the fiber are mounted at the middle disk in the same way as in the previous set-up, also the PEEK bottom disk stayed the same. The whole set-up is shown in the following rendered pictures 5.1 and 5.2.

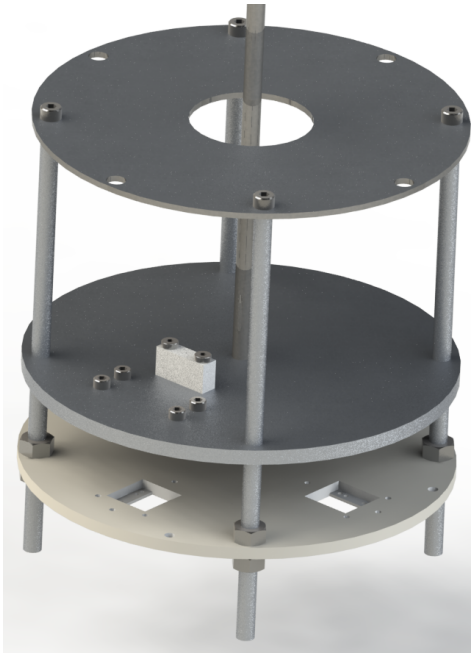

Fig. 5.1: First set-up version at nearly the lowest position. The holes in the top disk are for the mounting of the set-up into the vessel.

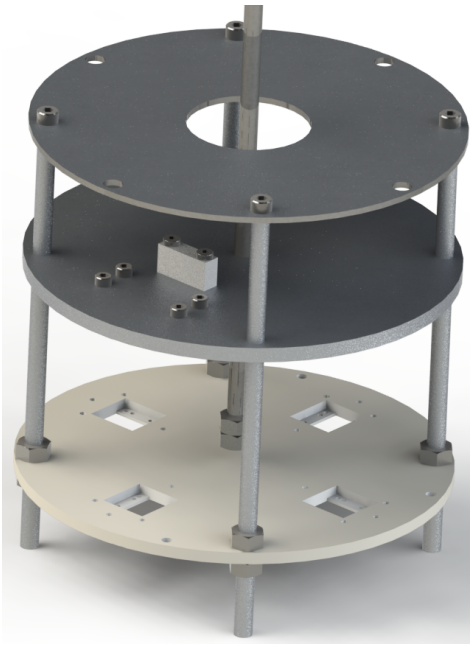

Fig. 5.2: First set-up version a little bit above the half height. The two nuts at the end of the middle rod are defining the minimum distance between bottom and middle disk.

The gap between the bottom disk and the end of the four guiding rods is a spacer for the cable bending and also not to block the xenon outlet. This first version allowed an absolute height of 150 mm.

After the first set-up was ready we did some "dry runs" to test the sliding property. Already in the first try it was clear that this set-up in this way would not work. Changing the height too fast ends up with the middle plate getting stuck. This was caused by two problems: on the one hand the guiding holes in the middle disk were to small and should be replaced by elongated holes. On the other hand the screwing of the guiding rods at the top disk is too susceptible to bending. To further ensure that the middle disk gets not stuck, for the final version we also decided to take into account that the linear thermal expansion coefficient for peek is around twice as high as for stainless steel. Thus an uneven shrinking during the cool down process would bend the guiding rods.

5.2 Improved set-up version for the test of multiple devices

Taking all this into account, a improved version was developed. In addition we started a collaboration with another SiPM producer, Ketek GmBh. Hence we have to adapt these devices to our set-up.

Since each measurement run takes several days for the cooling down, stabilizing the system, data taking and recuperation, it is advisable to measure more than just a single SiPM per run. Therefore the final version allows to measure four of them at the same time under the condition of equal illumination. In order to realize this with a single source it is necessary to have a lift- and rotatable system at once. Therefore the middle disk rotates while the bottom disk with the sensors is lifted. The realization of such a system is shown on the left.

Fig. 5.3: Model of the improved set-up. The letters are described in the text. See also appendix page 53 and 54

One big change is caused by the mentioned different thermal expansion coefficients. To avoid an uneven shrinking of the top and bottom disk, the bottom disk has been divided into two separated disks (A). The lower disk is made out of stainless steel with the same thickness just like the top disk (see also figure 5.4), whereas the upper bottom disk is still made of peek concerning the previously mentioned reasons (chapter 3.1).
In order to avoid the bending of the guiding rods the fixing mechanism was changed (B). The washers provide a more stable support to keep the rods perpendicular.
Spot (C) shows one of our two collimators, which are explained a bit later. They are designed according to the results of the simulation and are also made out of PEEK reducing the reflection probability.

At position (D) a dummy for the Ketek SiPM-PCB is shown, that can be fixed into the corresponding holder with screws. This has the advantage that one is not forced to solder e.g. some kind of holder pins directly to the bottom disk. Since the Hamamatsu SiPMs do not have such a PCB, it was also designed in Mainz. It is made out of PEEK as well and is shown in figure 5.4 at position 1 and in figure 5.5.

Fig. 5.4: Bottom view of the improved set-up. The number 1 marks the developed Hamamatsu SiPM PCB, whereas number 2 marks the one from Ketek.

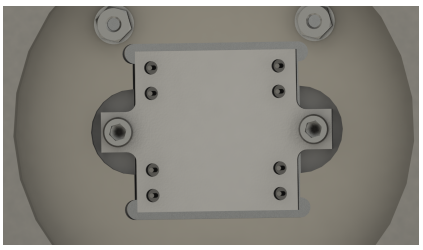

Fig. 5.5: Hamamatsu PCB inside its space holder at the downside of the PEEK disk.

Another major change was adapted from the old APD set-up, where it already has been tested successfully and represents the spring holders shown in spot (E1 in figure 5.3). Since the set-up is also rotatable, a new method to position the source well defined above the SiPMs is necessary. Therefore we are using a ball and the spring holder in addition with tiny indentations on the middle disk to fix the position (see figure 5.8). Those four spring holders are arranged at position 90° relative to each other. The hardness of each spring can be changed via a screw as shown in point (E2 in figure 5.3).

As before we are using PT-100s for the temperature measurement some. Since we had some trouble with the fixing during the first run we decided to place some additional threads into the PEEK disk (F fig. 5.3). A second PT-100 will be fixed at one guiding rod next to the rotatable middle disk by a piece of wire. In this way we have still the advantage to know the liquid level by comparing their different temperatures.

The last big point during the design process was the realization of a collimator system for both source and SiPM. There were mainly three reasons for that:

- Having a well-defined source right in the center of each channel.
- Reducing the illumination of the SiPM by reflected light.
- Getting rid of the dead pixels of the SiPM.

The effect of collimators have been investigated first with graphical beam path simulations with *Mathematica* and later a proper simulation with *C++* which has already been explained in chapter 4.2.
The first attempt was to have a little mask for the source and bigger collimator for the SiPM. The mask should include four holes each in a line with one channel of the SiPM. This idea is under the assumption that only through one of those four holes is within the measured time gate an α-particle emitted.

The collimator for the SiPM was a bit more complicated. It has also four holes for defining the solid angle and additionally a big body followed by a second collimator to catch cross-lighting and reflections. But already a simple reconstruction of the beam paths is showing that there are two drawbacks of such a collimator system, see fig. 5.6

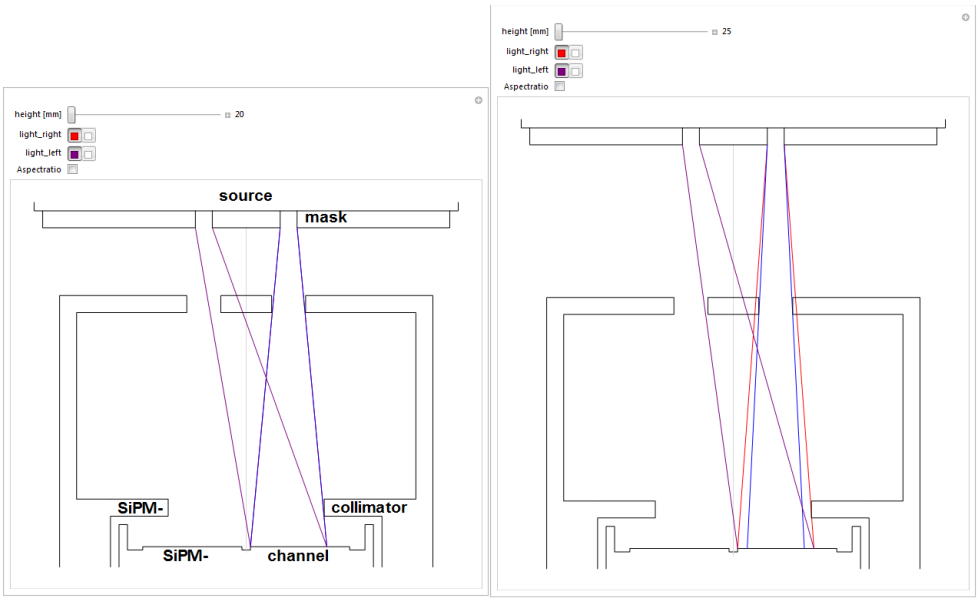

Fig. 5.6: *Mathematica* beam path side sketch for the first collimator idea at a height of 20 mm (left picture) and 25 mm (right picture). The different colors showing different beam paths, whereby the purple beam shows cross-lighting, the blue beam the path of the given height and the red one indicates the beam path for the same illuminated area as for 20 mm.

One drawback is the cross-lightning, see the the purple beam in fig. 5.6. But more crucial is the fact that the illuminated area changes with the height. A change of the illuminated area would cause a more difficult determination of the quantum efficiency. This beam cutoff is caused by the small openings of the SiPM collimator. Due to the fact that an expansion of this openings would also increase the cross-lighting and reflection lighting, we decided to have a more simple collimation system.

Therefore the source has been masked by a Kapton-foil just as before to reduce the diameter of the active area to 2.1 mm. Additionally the source will be enclosed by a collimator with a cavity and a central hole with a diameter of 4 mm, as shown in figures 5.7 and 5.8.

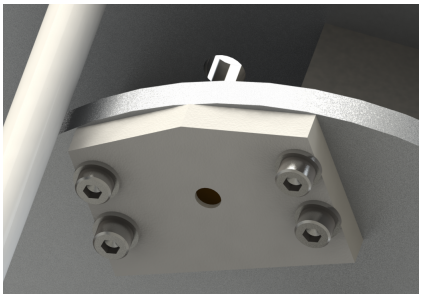

Fig. 5.7: *SolidWorks* model of the Source collimator. The edge cutoffs were needed to not collide with the guiding rods.

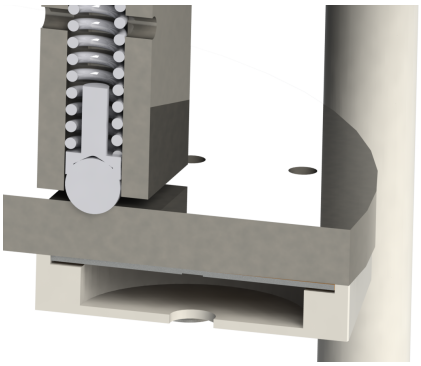

Fig. 5.8: Cross-section of the source collimator and one spring holder. The cavity of the source collimator has a height of 3.7 mm. The additional holes in the spring holder walls are for the evacuation.

The cavity of the collimator catches the light which is emitted in large angles, thus avoiding any reflections from the vessel walls.

Since the source collimator provides a well-defined beam the SiPM collimator has mainly the task to throw a shadow on the dead pixels and only secondly to get rid of any reaming reflections.Its height has been reduced that there is just a safety gap of 1 mm is between the surface of the quartz window of the SiPM and the collimator. Unfortunately we do not know which rows are the dead ones, so we decided to throw a shadow on the first 7 rows of each channel side to be sure. Hence the active area is reduced to $(5.8 \,\mathrm{x}\, 5.8)\,\mathrm{mm}^2$ and the total number of pixels to 13456. The CAD-model is shown in the two following figures 5.9 and 5.10.

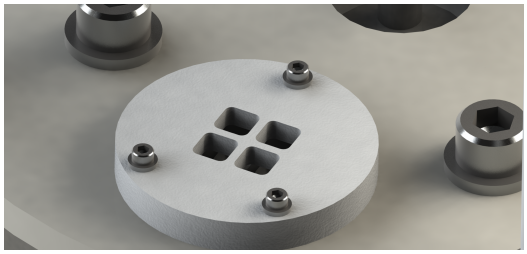

Fig. 5.9: CAD-model of the SiPM collimator. The inner edge roundings will during caused the manufacturing.

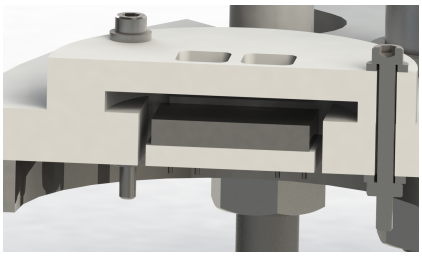

Fig. 5.10: Cross-section of the SiPM collimator together with the Hamamatsu SiPM-PCB and SiPM dummy.

With this final version we achieve a maximum height difference of 80 mm.
The simulation for the illumination yield of this system looks promising, fig. 5.12. The maximum height allows us to decrease the illumination yield from 605 ± 24(20 mm height) to 40 ± 6(80 mm height) photons in average (Fits of the peak spectra see appendix page 59 fig. 7.8 and 7.9). Furthermore shows the simulation that the multiple impinged photons can be assumed for the maximum height as 0.

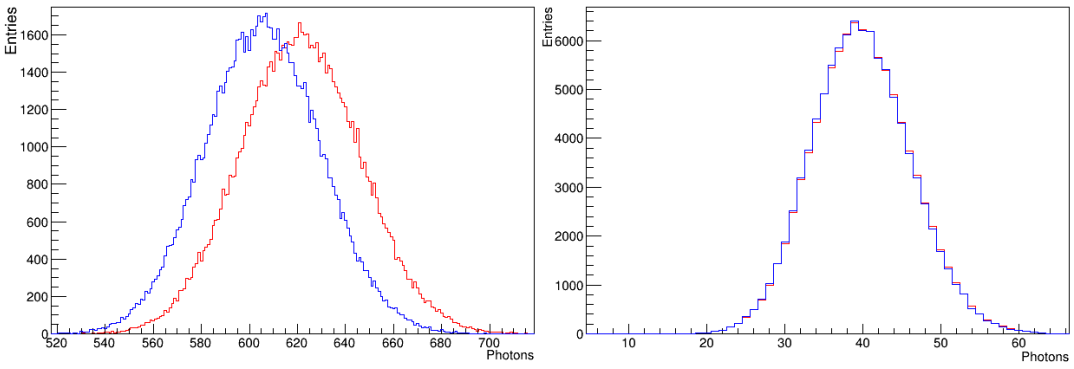

Fig. 5.11: Spectrum of the new system for the minimum height of 20 mm (left) and maximum height of 80 mm (right). The blue peak represents the detected photons, whereas the red peak shows the impinging photons.

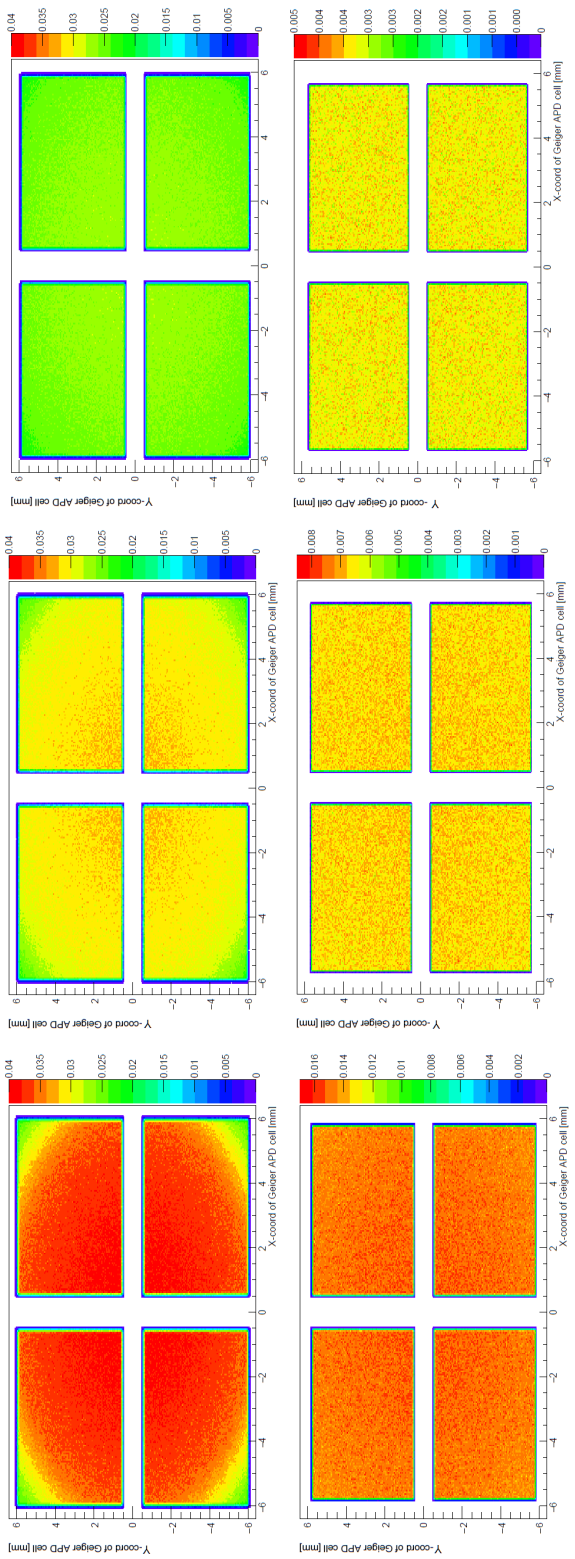

Fig. 5.12: Distribution of the illumination yield of the new set-up with a 30% PDE. The white area shows the cast shadow of the collimators. The first row shows the set-up in 25.0 mm, 27.5 mm and 30.0 mm height, whereas the second row shows the setup in 40 mm, 60 mm and 80 mm (maximum) height. One should also note that the second row sticks not to the same z-scale.

6 Summary and Acknowledgment

During this bachelor thesis it was possible to reuse an already existing set-up for a completely new task. We prepared the old cooling and recirculation system to get a closed and working gas system which guarantee a constant purity level of our xenon. Furthermore it allows us to fill and recuperated the xenon to and from our sealed measurement vessel. In addition with the realized circuits for the supply and read out of the SiPMs, we prepared all required conditions for an initial test run.

During this test run we used an already existing measurement set-up for the characterization of APDs, to test one of our SiPMs. Although a new and improved system has been developed in this thesis and it will be manufactured soon. It fits to the new challenges for the characterization of SiPMs and it allows us to vary the illumination yield between the starting condition with a value of N_0 to the end conditions with a value of $N_0/16$. Furthermore it supports the characterization of 4 SiPMs during the same measurement. Hence the acquisition of the data is done under the same conditions which is important for a comprehensive of the SiPMs. With its changeable collimation system nearly each SiPM geometry can be tested and if needed the illumination yield can be increased, or decreased further.

With the already existing APD set-up in addition with the written simulation from Doctor Matteo Alfonsi and the analysis approach of the photo detection efficiency, it was possible to do a first representation of the data from the initial test run.

With the establishment of the SiPM characterization setting and the initial test run is an important step done. Although the initial measurement seems not to provide the final goal of the determination of the photon detection efficiency, it proved us the operational readiness of the most parts. Some minor issues needs to be fixed in the following weeks, to acquire a better set of data during the next measurement run. Furthermore needs the new measurement set-up to be manufactured and tested in some dry-runs with a Dewar and liquid nitrogen.

I think in total we can suppose, that the test setting is on a good way and the final characterization of SiPMs will be done soon in the future.

Working on this project was a lot of fun. I learned much about the development of an Experiment in addition with a lot of stuff about cryogenics and the careful behavior with xenon as scintillation medium.

Additional provided me the simulation an insight into *C++* which I would like to develop.

At the end i would like to thank Professor Oberlack for the offer to write my thesis in his group and his support during it.
Furthermore i am very thankful for the great assistance and motivation of Doctor Matteo Alfonsi.
Closing I want to thank Christopher Hils and Melanie Scheibelhut, who supported me with the night shifts during the measurement and the rest of the xenon group of their encourage and supporting way.

7 Appendix

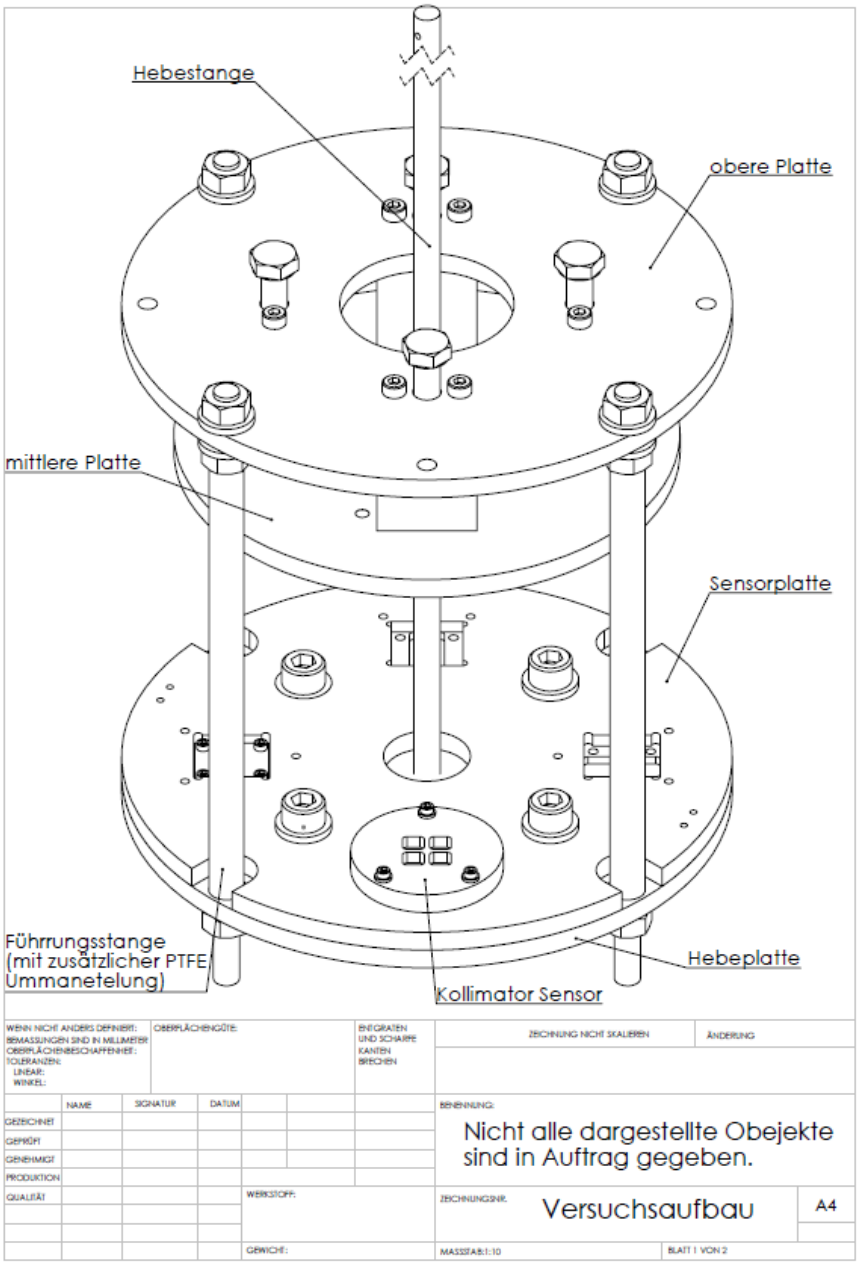

Fig. 7.1: Isometric sketch for the workshop of new set-up (topview).

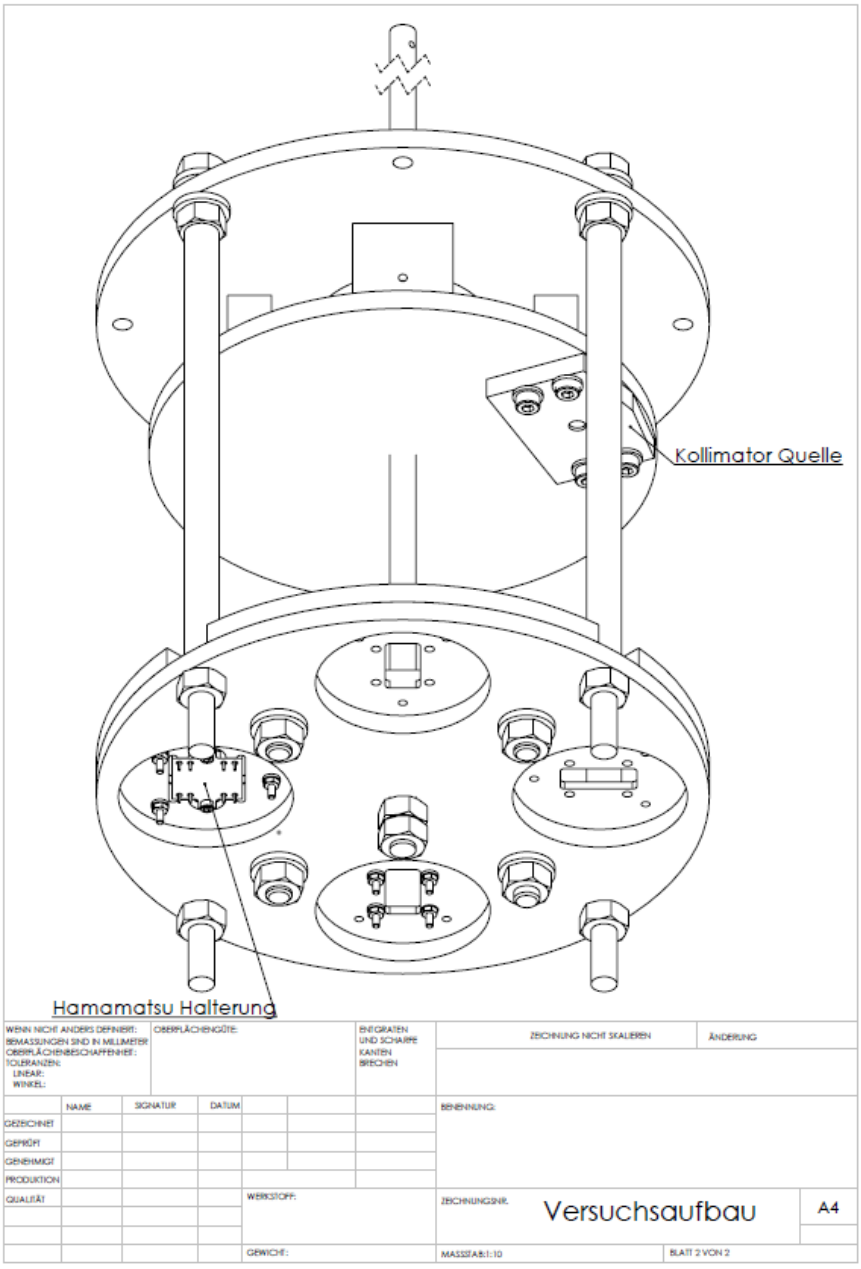

Fig. 7.2: Isometric sketch for the workshop of new set-up (bottom view).

S10943-3186(X) TENTATIVE SPECIFICATIONS

■Specifications (Ta=25 deg C)

Parameter	Symbol	Condition	min	typ	max	Unit
Spectral response Range			--	130～900	--	nm
Peak sensitivity wavelength			--	430	--	nm
Pixel pitch			--	50	--	um
Effective photosensitive area /channel		Device Type A	--	5.95 x 5.85	--	mm^2
		Type B	--	5.70 x 5.60	--	mm^2
Recommended operating voltage range *2	Vop	at M=1.25×10^6	60	70	80	V
Vop variation between channels			--	0.3	0.5	V
Temperature coefficient of reverse voltage			--	60	--	mV/deg C
Detection efficiency *3	PDE	VR=V(M=1.25×10^6) λ=175nm, in a vacuum	20	25	--	%
Dark count/channel *4	ID	VR=Vop				
		Device Type A	--	7.0	21.0	MHz
		Type B	--	6.4	19.2	MHz
Terminal capacitance/channel	Ct	VR=V(M=1.25×10^6)				
		Device Type A	--	1200	--	pF
		Type B	--	1100	--	pF
Gain at Vop	M	VR=Vop	--	1.25×10^6	--	--

*2 Refer to the attached data for recommended operation voltage of each product.

*3 The detection efficiency acquired by photocurrent is affected by optical cross talks and after pulses.

*4 The dark current is attached to each product.

Fig. 7.3: Hamamatsu Photonics SiPM Data sheet (first page). Note that we own SiPM Type A.

■Dimensional outlines (mm)

Type A

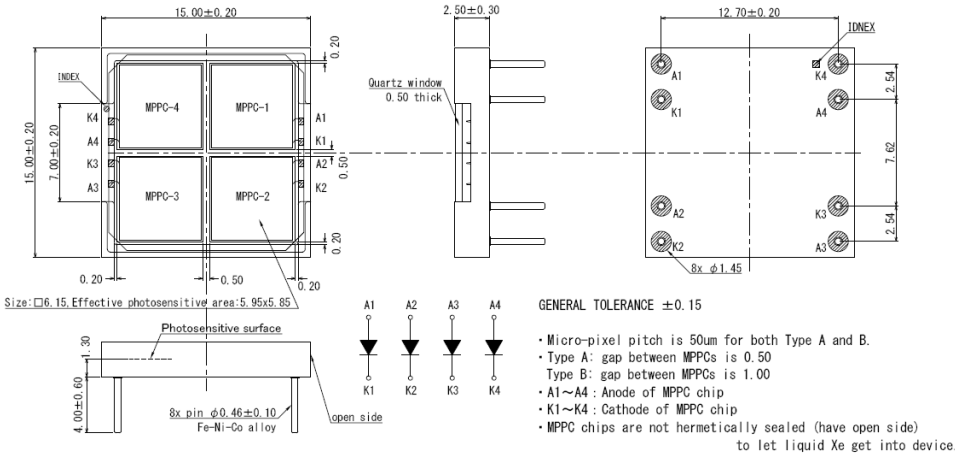

Type B

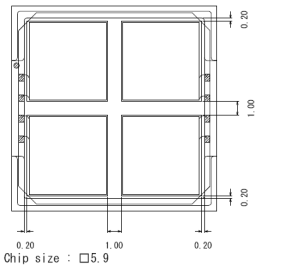

Fig. 7.4: Hamamatsu Photonics SiPM Data sheet (last page). Note that we own SiPM Type A.

FINAL INSPECTION SHEET	TypeNo.	S10943-3186(X)/NG	page	2/ 2
	Note			

Serial No.	ch.No	Vop [V]	Id[uA]
AA00065	1	66.78	1.03
	2	66.59	4.38
	3	66.77	9.60
	4	66.69	1.69
AA00137	1	66.84	1.91
	2	66.88	1.78
	3	66.74	1.88
	4	66.83	14.25

HAMAMATSU

Form K30-2033

Fig. 7.5: Hamamatsu Photonics SiPM specification of our two test SiPMs

Acquisition: Sampling Mode real time, Normal
Memory Depth manual 20.000 kpts
Sampling Rate manual 1.00 GSa/s
Averaging off, Interpolation Off

Channel 2: Scale 20.0 mV/, Offset -51.2 mV, Skew 0.0 s
Coupling DC, Impedance 1 MΩ

Channel 3: Scale 20.0 mV/, Offset -78.0 mV, Skew 0.0 s
Coupling DC, Impedance 1 MΩ

Channel 4: Scale 20.0 mV/, Offset -22.0 mV, Skew 0.0 s
Coupling DC, Impedance 1 MΩ

Horizontal: Scale 100 ns/, Position 0.0 s, Reference center

Trigger: Mode Pattern/State, Pattern [X L L L]
Trigger When entered
Chan 2 Level -2.0 mV, Chan 3 Level -2.0 mV, Chan 4 Level -2.0 mV
Sweep triggered, Sensitivity normal, Holdoff Time 100 ns

Measure:

	Area(2)	DCVrms(2)	V p-p(2)	DCVrms(4)	V p-p(4)
Current	-9.91572 nVs	24.1526 mV	119.688 mV	11.8469 mV	60.670 mV
Mean	-4.89003 nVs	11.1101 mV	54.9314 mV	? 9.16821 mV	? 45.7020 mV
Min	-10.5862 nVs	4.97759 mV	25.417 mV	? 3.42079 mV	? 17.567 mV
Max	-2.34270 nVs	25.4674 mV	124.694 mV	? 22.5277 mV	? 103.844 mV
Range (Max-Min)	8.24346 nVs	20.4898 mV	99.277 mV	? 19.1069 mV	? 86.278 mV
Std Deviation	2.78343 nVs	6.96730 mV	34.0174 mV	? 4.18493 mV	? 19.0866 mV
Number of Meas	17	17	17	17	17
Meas Window	Area(2)	Main	Main	Main	Main

Fig. 7.6: "Screen shot" of the oscilloscope. In the text under the screen are the used parameters for the measurement.

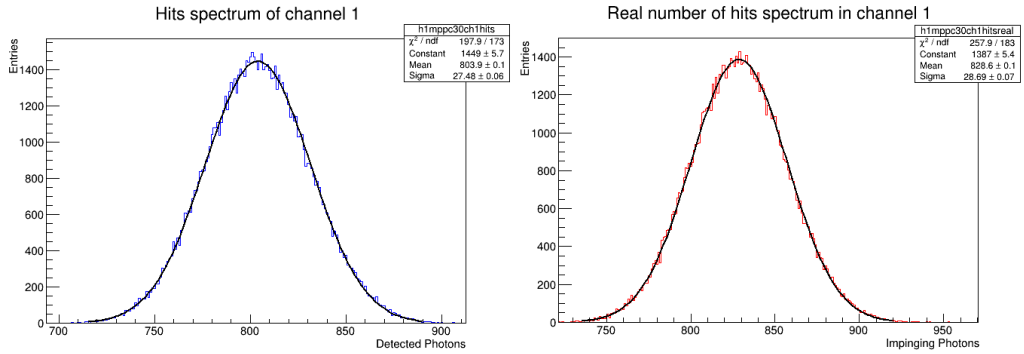

Fig. 7.7: Fits of the simulated hit spectrum for the already existing measurement set-up.

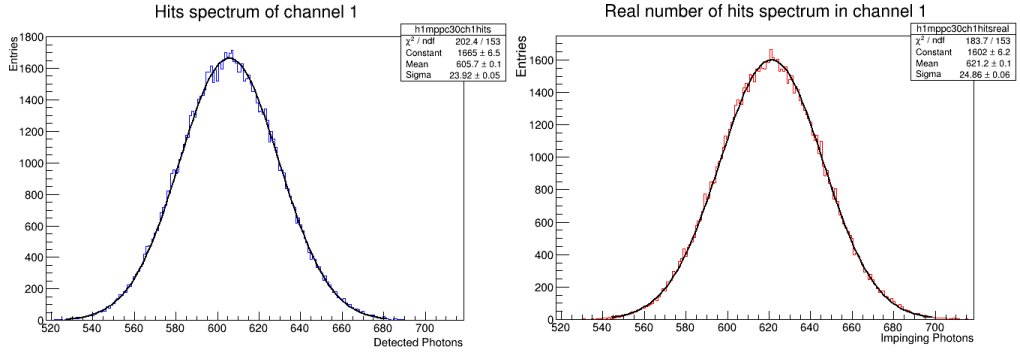

Fig. 7.8: Fits of the simulated hit spectrum for the already new measurement set-up, at 20 mm.

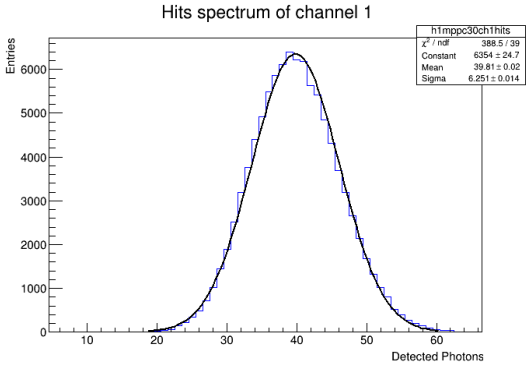

Fig. 7.9: Fits of the simulated hit spectrum for the already existing measurement set-up, at 80 mm.

Bibliography

[1] W. Demtröder, *Experimentalphysik 3* (4. edition) , Springer Verlag Berlin Heidelberg (2010)

[2] W. Demtröder, *Experimentalphysik 4*, Springer Verlag Berlin Heidelberg (2013)

[3] Harald Ibach and Hans Lüth, *Festkörperphysik: Einführung in die Grundlagen* (7. edition), Spinger Verlag Berlin Heidelberg (2009)

[4] Glenn F. Knoll, *Radiation Detection and Measurement*, John Wiley & Sons, Inc (2000)

[5] P.K. Lightfoot et. al., *Characterisation of a silicon photomultiplier device for applications in liquid argon based neutrino physics and dark matter searches*, IOP PUBLISHING AND SISSA (2008)

[6] Claudio Piemonte *A new Silicon Photomultiplier for blue light detection*, Nuclear Instruments and Methods in Physics Research A 568 (2006) 224-232

[7] Vitaly Chepel and Henrique Araújo, *Liquid noble gas detectors for low energy particle physics*, JINST 8 R04001 (2013)

[8] W. Ootani et. al., *Development of deep-UV sensitive MPPC for liquid xenon scintillation detector*, Nuclear Instruments and Methods in Physics Research A 787 (2015) 220-223

[9] E. Aprile and T. Doke, *Liquid xenon detectors for particle physics and astrophysics*, REVIEW OF MODERN PHYSICS, VOLUME 82, JULY-SEPTEMBER 2010

[10] Muller, M. E. *A Note on a Method for Generating Points Uniformly on N-Dimensional Spheres.* Comm. Assoc. Comput. Mach. 2, 19-20, Apr. 1959.

[11] MPPC and MPPC module for precision measurement, Hamamatsu Photonics, August 2014

[12] Matthias Morbitzer, *Aufbau einer Testkammer zur Charakterisierung von Avalanche-Photodioden für eine flüssig Xenon TPC*, 26.10.2012

[13] NIST Chemistry WebBook, `webbook.nist.gov/chemistry/`, (07.11.2014 10:38)

[14] NASA *Outgassing Data for Selecting Spacecraft Materials*, `outgassing.nasa.gov/cgi/uncgi/search/search.sh`, (22.05.2015 08:40)

[15] Cern Courier *Silicon photomultiplier demonstrates its capabilities*, erncourier.com/cws/article/cern/28805, (14.06.2015 15:31)

[16] Agilent Ininiium 9000 Series Oscilloscopes Data sheet, http://cp.literature.agilent.com/litweb/pdf/5990-3746EN.pdf, (14.06.2015 20:21)

[17] User:Cepheiden, *Leitungsmechanismen im dotierten und undotierten Halbleiter in Abhängigkeit von der Temperatur*, http://de.wikipedia.org/wiki/Halbleiter, (15.04.2015 17:20)

[18] User:TheNoise, *Pn-junction-equilibrium.png*, http://en.wikipedia.org/wiki/File:Pn-junction-equilibrium.png, (14.04.2015 20:01), (Had been adapt under terms of the GNU Free Documentation License.) (change: some labeling)

[19] User:Kirnehkrib, *Si-Avalanche-Photo-Diode (APD)*, http://de.wikipedia.org/wiki/Datei:APD2_German.png (05.06.2015 12:24)

[20] User:Kirnehkrib, *harge carrier multiplication in a Si-Avalanche-Photo-Diode (APD)*, http://de.wikipedia.org/wiki/Datei:APD3_German.png (05.06.2015 12:28), (Had been adapt under terms of the Creative-Commons-License)

[21] *Energy band diagram of a p-n junction in thermal equilibrium*, http://ecee.colorado.edu/~bart/book/book/chapter4/ch4_2.htm (05.06.2015 11:58)